User Detection in RIS-based mmWave JCAS: Concept and Demonstration

Yueheng Li, Lucas Giroto de Oliveira, *Graduate Student Member, IEEE*, Axel Diewald, Xueyun Long, Elizabeth Bekker, *Graduate Student Member, IEEE*, David Brunner, Xiang Wan, *Senior Member, IEEE*, Tie Jun Cui, *Fellow, IEEE*, Thomas Zwick, *Fellow, IEEE*, and Benjamin Nuss, *Senior Member, IEEE*

***Abstract*—In this article, joint communication and sensing (JCAS) is combined with reconfigurable intelligent surfaces (RISs), which validates a novel RIS-based JCAS (RIS-JCAS) system. The proposed system performs monostatic sensing to detect a potential user, after which communication with the user is established. The corresponding RIS-cascaded channel is formulated, based on which an algorithm is created, to handle radar target detection and communication channel estimation while multiple RISs operate simultaneously. A joint beam training process by utilizing the identical beamforming pattern on multiple RISs is created, which increases the time efficiency significantly. The detection accuracy is subsequently further improved through a novel fine-tuning method. To practically validate the aforementioned algorithm, a RIS-JCAS system is demonstrated using a mmWave testbed with a bandwidth of 1 GHz centralized at 26.2 GHz. Besides combining the widely adopted orthogonal frequency-division multiplexing (OFDM) scheme with high-directional RIS beams, the system also allows the use of variant RIS flat-top beam shaping combined with orthogonal chirp-division multiplexing radar (OCDM) waveforms. This idea keeps the sensitivity of the RIS-JCAS system while broader beams with wider coverage but lower gain are utilized. Overall, accurate 4-dimensional sensing results are derived, which strongly assists the communication channel estimation and realizes the core benefits of the proposed RIS-JCAS system.**

***Index Terms*—Joint communication and sensing, millimeter wave, reconfigurable intelligent surface**

I. Introduction

Radar and communication applications have been playing important roles in our daily lives since the beginning of the 21st century. Radar technologies have been implemented in the automotive industry for safe driving [1]. Besides the standard orthogonal frequency-division multiplexing (OFDM) radar in [2], other waveforms with variant features, such as orthogonal chirp-division multiplexing (OCDM) in [3], [4], have also been studied to satisfy different requirements. Communication technologies are developing toward 6th generation mobile networks, with impressive research topics including millimeter wave (mmWave) communication [5], massive multiple-input multiple-output (MIMO) [6], [7], etc. As a general demand, both radar and communication applications occupy more spectrum, power, and hardware resources to improve their system performances, which leads to allocation conflicts. As a solution, the concept of joint communication and sensing (JCAS) is raised and studied in [8], [9], to combine both technologies by sharing the hardware chain, signal processing scheme, and bandwidth.

Although JCAS reuses the common parts of radar and communication systems as much as possible, the cost and power consumption could still be problematic, especially at mmWave frequencies, when the fabrication is more challenging and free space path loss (FSPL) is stronger. Therefore, finding solutions to realize low-cost systems while maintaining proper performance has been one of the essential topics in the last few years. One of the most promising approaches entails the use of reconfigurable intelligent surface (RIS) [10], which is also known as programmable metasurface (PM) or intelligent reflecting surface (IRS) [11]. As an alternative antenna array, a RIS is illuminated by electromagnetic (EM) waves from a feeding source over the air. By switching the operation states of electronically controllable micro-components on the RIS unit cells, the EM wave can be further propagated to achieve beam shaping and beam steering. Compared to conventional antenna arrays, the aforementioned RIS architecture brings low-cost benefits due to using cheap and low-power micro-components. Meanwhile, free-space illumination is utilized instead of complex analog circuitry to ease the design complexity. This further leads to the property that an RIS is a uniform planar array (UPA) that can be placed flexibly, for example, attached to the wall of a building. Motivated by these advantages, promising RIS designs have been demonstrated during the past few years in [10], [12]–[14] with different illumination types, using different micro-components, and having different phase resolutions. Among the aforementioned options, this article focuses on the 1-bit reflect array RIS-based on PIN-diodes, which maximizes the low-cost property, especially for mmWave demonstration, as reported in [15], [16].

So far, the RIS concept has been widely merged with wireless communication technologies. At the theoretical level, RISs can work as promising relay nodes that increase the scattering for higher channel capacity [11], or provide a robust wireless communication link, even if the line-of-sight (LoS) between the base station (BS) and user equipment (UE) is blocked by obstructions [17]–[19], or support internet-of-things (IoT) related technologies [20]. The authors of [21] creatively proposed the concept of the refracting RIS and applied it to the hybrid satellite-terrestrial relay network architecture to overcome the serious penetration loss effect with mmWave signals, which greatly improved the coverage of satellite networks. In [22], the authors first studied the suppressing effect of the malicious RIS on the system performance. They conducted

the cooperative and uncooperative optimization designs from multiple perspectives of whether the legitimate transmitter is aware of the identity of malicious RIS. In practice, the aforementioned RIS theories are proved in [23]. In addition, RIS's ability to provide real-time mobile communication and multiuser access is studied in [15], [24]. On the other hand, the study of RIS in a radar system is only at the theoretical level [25]–[27]. In principle, due to the hardware and signal-sharing property of communication and radar systems, the RIS also has the potential to benefit radar processing, therefore supporting the entire JCAS system. This leads to a RIS-based JCAS system (RIS-JCAS) as discussed in theoretical analysis in [28]–[30]. However, due to the RIS properties, it brings the challenges of massive unit cells, no amplitude control, and low phase resolution into the system, as mentioned in [16]. These challenges have to be solved to realize a RIS-JCAS system with proper performance.

This article addresses several of the aforementioned open aspects and demonstrates the realization of a RIS-JCAS system for concept and demonstration. The major contributions can be summarized as follows:

- System concept formulation and measurement-based validation of a RIS-JCAS system consisting of a JCAS base station (BS) assisted by RISs, which performs monostatic radar sensing to detect a potential user and communicate with it. The corresponding RIS-cascaded radar and communication channels, together with the link budget, can be future references for related system models.
- Sensing-assisted communication algorithm design to handle radar target detection and communication channel estimation, with multiple RISs operating simultaneously. A joint beam training process is created for the Tx and Rx RISs which increases the time efficiency significantly. The detection accuracy is subsequently further improved through a novel fine-tuning method. Overall, accurate 4-dimensional (4D) sensing results, including range, velocity, and two spherical angles, are derived, which strongly assists the communication channel estimation and realizes the core benefits of the proposed RIS-JCAS system.
- RIS-JCAS system demonstration using a mmWave testbed with a bandwidth of $1\,\mathrm{GHz}$ centralized at $26.2\,\mathrm{GHz}$. In the adopted testbed, the 1-bit PIN-diode-based RISs from [12] are used, which cover the licensed 5G 3GPP bands with surplus bandwidth for future applications. Besides combining the widely adopted OFDM scheme with high-directional RIS beams, the demonstrated system also allows the use of variant RIS flat-topped beam shaping strategies combined with OCDM radar waveforms. This idea maintains the sensitivity and time efficiency of the RIS-JCAS system while broader beams are utilized.

Throughout this article, $(\cdot)^T$ denotes the transpose of a matrix or vector. The operator $\angle$ indicates the phase angle. $\boldsymbol{A} = \mathrm{diag}(\boldsymbol{a})$ means $\boldsymbol{A}$ is a diagonal matrix with the elements filled by $\boldsymbol{a}$. The operators argmin and argmax denote the arguments of the minima and maxima, respectively. Parameter definitions are mentioned in some figure captions, so a joint reading with the texts is suggested.

II. Problem Statement

A. RIS-JCAS System Model

The proposed RIS-JCAS system in this article is depicted in Fig. 1(a). The BS and RIS perform quasi-monostatic sensing, while the UE is both a target for the BS to sense as well as a downlink communication receiver (Rx). Considering the LoS path between the BS and UE is not available, the sensing channel is assisted by an UPA transmitter (Tx) RIS reflecting the signal from the BS Tx to the UE, and an UPA Rx RIS reflecting the signal from the UE back to the BS Rx. After the UE is detected via the sensing channel, the BS communicates with it via the Tx RIS. The Tx and Rx are distributed with different RISs to ensure the best beamforming pattern for the RISs, and avoid strong mutual coupling between the Tx and Rx via a single RIS. Depending on the distance between the source antenna and RIS, there are two possible approaches. In the first case, RISs can be seen as low-cost novel antenna arrays, having their beamforming gains maximized with the BS antennas in close range, mainly pointing to the phase center of the RISs. In the second case, RISs behave as reflective relays, creating promising paths between the BS and UE, while obstacles such as trees and buildings in urban city scenarios block the LoS path between them. The aforementioned cases are concluded to be nearfield and farfield illuminated RIS beamforming in [31]. The authors also proved that both approaches share a general path model. In [23], it is further studied that the two approaches can be described using one general channel model for signal processing algorithm designs, therefore being jointly considered in this article. In addition, Tx and Rx with a single antenna are considered, but array processing is also possible with extensions.

As shown in Fig. 1(a), the main sensing cascaded path includes four parts in a row: from Tx to Tx RIS, from Tx RIS to UE, from UE to Rx RIS, and from Rx RIS to Rx denoted by $\boldsymbol{h}_p = [\alpha_{p,1}e^{j\omega_{p,1}}, \alpha_{p,2}e^{j\omega_{p,2}}, ..., \alpha_{p,k}e^{j\omega_{p,k}}, ..., \alpha_{p,K}e^{j\omega_{p,K}}]$ with path index p. This channel coefficient is defined for every subcarrier $n_\mathrm{c} \in \{0, 1, \ldots, N_\mathrm{c}\}$, out of the total N_c subcarriers. For the sake of conciseness, the subcarrier index is henceforth omitted. The term $K = M \times N$ denotes the number of RIS unit cells with $M_\mathrm{Tx} \times N_\mathrm{Tx}$ when the channels are related with the Tx RIS, yielding $p \in \boldsymbol{p_{\mathbf{Tx}}} = \{p_1, p_2\}$. Similarly, $M \times N = M_\mathrm{Rx} \times N_\mathrm{Rx}$ for channels related to Rx RIS, yielding $p \in \boldsymbol{p_{\mathbf{Rx}}} = \{p_3, p_4\}$. From the K unit cells, the $k\mathrm{th}$ one, with $k = [N(m-1)+n] \in \{1, 2, \ldots, K\}$ having $m \in \{1, \ldots, M\}$ and $n \in \{1, \ldots, N\}$, has an attenuation factor $\alpha_{p,k} \in \mathbb{R} \geq 0$ caused by the path loss, antenna gain, radiation coefficient, etc. The phase $\omega_{p,k} \in [0, 2\pi)$ is introduced by the geometric position of the unit cells, causing discrete propagation delays. In general, $\omega_{p,k} = \kappa r'_{p,k} = \kappa r_p + \kappa r_{p,k} = \psi_p + \psi_{p,k}$, with the wave number $\kappa = 2\pi/\lambda$, having $\lambda = c_0/f_\mathrm{c}$ as the wavelength at the carrier frequency f_c. Based on the phase centers, $r'_{p,k}$ is the distance between the reference antenna to the $k\mathrm{th}$ RIS unit cell. This can be further expressed by a general path distance r_p from the reference antenna to the phase center of the RIS, plus an individual variant distance

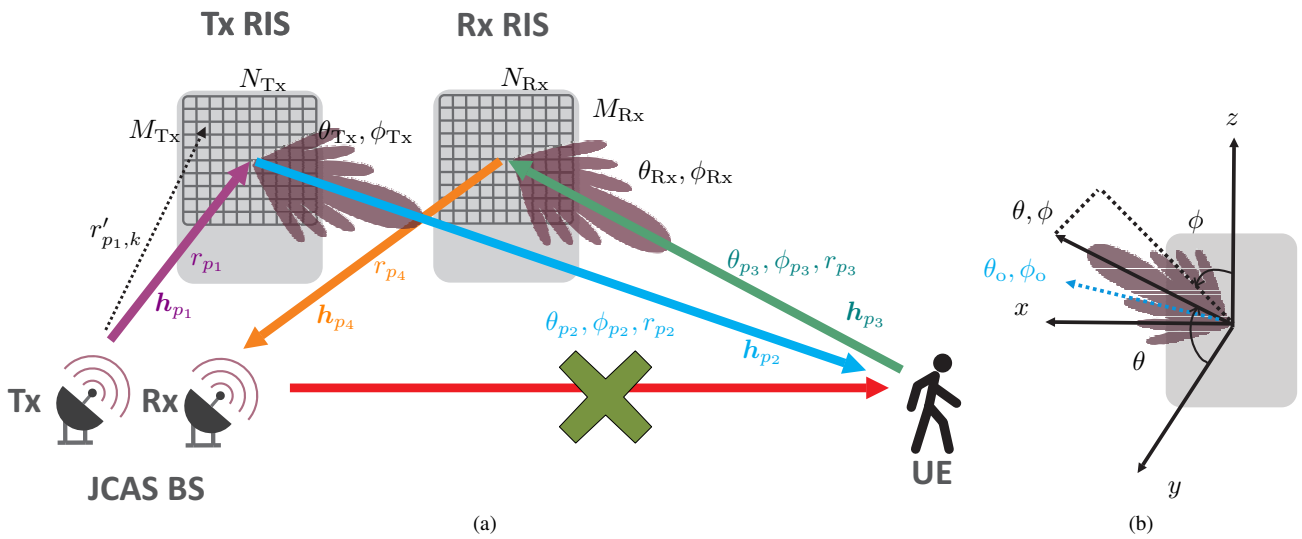

Fig. 1. (a) System model of the proposed RIS-JCAS system. Each step of the cascaded channel is $\boldsymbol{h}_p$, with the path index indicated by $p \in \boldsymbol{p} = \{\mathrm{Tx} \rightarrow \mathrm{RIS_{Tx}}, \mathrm{RIS_{Tx}} \rightarrow \mathrm{UE}, \mathrm{UE} \rightarrow \mathrm{RIS_{Rx}}, \mathrm{RIS_{Rx}} \rightarrow \mathrm{Rx}\} = \{p_1, p_2, p_3, p_4\}$. The Tx RIS has $M_{\mathrm{Tx}} \times N_{\mathrm{Tx}}$ unit cells and the Rx RIS has $M_{\mathrm{Rx}} \times N_{\mathrm{Rx}}$ unit cells. The path distance is expressed by r_p, and the propagation distance for each RIS unit cell is $r'_{p,k}$ using $r'_{p_1,k}$ as an example. The direction of deparature/arrival (DoD/DoA) angles are θ_p, ϕ_p. The beamforming generated by RIS is pointing to θ_{Tx}, ϕ_{Tx} for Tx, and θ_{Rx}, ϕ_{Rx} for Rx, yielding the case that the system performance is optimized if θ_{Tx}, ϕ_{Tx} and θ_{Tx}, ϕ_{Tx} match with the corresponding θ_p, ϕ_p. (b) 3D Coordinate for the RIS beamforming. The beamforming direction is denoted by θ, ϕ. The angle θ is the opening angle between the beamforming direction and the y-axis, the angle ϕ is the angle between z axis and the beamforming direction contribution on the xz plane, where the RIS is placed. The observation direction for the antenna gain are $\theta_{\mathrm{o}}, \phi_{\mathrm{o}}$ expressed by the blue dashed line.

$r_{p,k}$ as a small-scale unit cell position adjustment. The general path distance r_p leads to the common phase shift of ψ_p, and the individual variant distance $r_{p,k}$ leads to the phase difference between the unit cells $\psi_{p,k}$. The latter one can be further discussed in two cases as

$$\psi_{p,k} = \begin{cases} \kappa r_{p,k}, & p \in \boldsymbol{p}_{\mathbf{BS}} \\ [(n-a)\sin\theta_p\cos\phi_p + \\ (m-b)\sin\theta_p\sin\phi_p]\kappa d, & p \in \boldsymbol{p}_{\mathbf{UE}}. \end{cases} \tag{1}$$

For the paths related to the BS, $\boldsymbol{p}_{\mathbf{BS}} = \{p_1, p_4\}$, $\psi_{p,k}$ is caused by the variant distance $r_{p,k}$ from the BS reference antennas to each RIS unit cell, depending on their geometric positions. As mentioned in [23], [31], such phase differences have more gradients when the BS antennas are close to the RIS. They become more uniform when the BS antennas are placed further away, with the EM wave converging to quasi plane wave with an incidence angle. This is also one of the major differences between the aforementioned nearfield and farfield illuminated RIS beamforming approaches when expressed by one general equation. For the paths related to UE, $\boldsymbol{p}_{\mathbf{UE}} = \{p_2, p_3\}$, $\psi_{p,k}$ is a steering vector related to the unit cell indexes as well as the DoD/DoA angles using the RIS surface as the reference plane. The constant d is the distance between the RIS unit cells. The terms a and b are equal to $1/2$ or 0 when N and M are even or odd numbers, respectively.

Therefore, by multiplying $\boldsymbol{h}_p$ through all paths in $\boldsymbol{p}$, the cascaded sensing channel coefficient is expressed as

$$h_{\mathrm{s}}(r_{p_1,k}, r_{p_4,k}, \theta_{p_2}, \theta_{p_3}, \phi_{p_2}, \phi_{p_3}) = \boldsymbol{h}_{p_4}\boldsymbol{h}_{p_3}^T\boldsymbol{h}_{p_2}\boldsymbol{h}_{p_1}^T \tag{2}$$

Considering practical applications, RIS size is unchanged and signal processing can measure the total propagation delay to derive ψ_p, therefore, the relative positions of the BS, RIS, and UE are the main interested parameters that are determined by the various distances and DoD/DoA in h_s. Following a similar logic, the cascaded communication channel coefficient is a part of the sensing channel h_s up to the UE, which is

$$h_{\mathrm{c}}(r_{p_1,k}, \theta_{p_2}, \phi_{p_2}) = \boldsymbol{h}_{p_2}\boldsymbol{h}_{p_1}^T. \tag{3}$$

B. RIS Beamforming in JCAS

In the previous section, the channel coefficients (2) and (3) are formulated considering a normalized RIS reflection. To successfully realize the JCAS functions, the RIS beamforming has to be designed properly. Based on [12], [15], the RIS beamforming has to consider the phase contributions in (1), which leads to

$$\begin{aligned} \varphi_k^{\mathrm{ideal}}(\theta, \phi) &= -[(n-a)\sin\theta\cos\phi + \\ &\quad (m-b)\sin\theta\sin\phi]\kappa d - \kappa r_{p,k} \\ &= \varphi_{\mathrm{ste}}(k, \theta, \phi) + \varphi_{\mathrm{dis}}(r_{p,k}), \end{aligned} \tag{4}$$

showing the phase shift at the kth RIS unit cell for the ideal case. Following the coordinate definition in Fig. 1(b), this means the RIS is aligning single beamforming to the direction θ, ϕ using the steering phase $\varphi_{\mathrm{ste}}(k, \theta, \phi)$ similar to the $p \in \boldsymbol{p}_{\mathbf{UE}}$ case in (1), and the distance phase introduced by $r_{p,k}$ in the $p \in \boldsymbol{p}_{\mathbf{BS}}$ case from (1) is compensated by $\varphi_{\mathrm{dis}}(r_{p,k})$. Considering the RIS design's low cost and power consumption requirements, this usually leads to the use of a L-bit phase shifted unit cell instead of a continuous phase shift. The limited phase resolution divides the $[0, 2\pi)$ range uniformly into 2^L slots, with hard decisions to determine the final unit cell phase shift $\varphi_k(\theta, \phi) \in \{0, 2\pi/2^L, (l-1)2\pi/2^L, ..., (2^L-1)2\pi/2^L\} + \varphi_{\mathrm{ref}}$, having $l \in \{0, 1, ..., 2^L - 1\}$ the phase index and φ_{ref} a flexible tuning value. Afterwards, the RIS beamforming matrix

$$G_{\mathrm{RIS}}(\theta,\phi,\theta_{\mathrm{o}},\phi_{\mathrm{o}})=\eta\frac{4\pi\left|E\left(\theta,\phi,\theta_{\mathrm{o}},\phi_{\mathrm{o}}\right)\right|^{2}}{\int_{0}^{\pi}\int_{-\pi/2}^{\pi/2}\left|E\left(\theta,\phi,\theta_{\mathrm{o}},\phi_{\mathrm{o}}\right)\right|^{2}\sin\theta_{\mathrm{o}}\mathrm{d}\theta_{\mathrm{o}}\mathrm{d}\phi_{\mathrm{o}}},\tag{7}$$

$\boldsymbol{\Phi}=\mathrm{diag}\left[e^{j\varphi_1(\theta,\phi)},e^{j\varphi_2(\theta,\phi)},...,e^{j\varphi_k(\theta,\phi)},...,e^{j\varphi_K(\theta,\phi)}\right]$ is obtained. This matrix model considers that the RIS unit cells have no amplitude tuning and only a phase shift ability [31], yielding a highly probable RIS unit cell design.

Based on (4) and according to [15], the farfield pattern of the RIS beamforming can be expressed as

$$\begin{aligned}E\left(\theta,\phi,\theta_{\mathrm{o}},\phi_{\mathrm{o}}\right)=\alpha_{\mathrm{RIS}}\sum_{k=1}^{K}\exp\{j\left[\varphi_k\left(\theta,\phi\right)\right.\\+\kappa d\left(n-a\right)\sin\theta_{\mathrm{o}}\cos\phi_{\mathrm{o}}\\\left.+\kappa d\left(m-b\right)\sin\theta_{\mathrm{o}}\sin\phi_{\mathrm{o}}\right]\},\end{aligned}\tag{5}$$

which shows the electric field strength observing at the direction $\theta_{\mathrm{o}},\phi_{\mathrm{o}}$, while the RIS is beamforming to θ,ϕ. The term α_{RIS} is a weighting factor that has been deeply discussed in [31]. As a summary, it can be written as

$$\alpha_{\mathrm{RIS}}=\sqrt{G_{\mathrm{f}}\left(\frac{\lambda}{4\pi}\right)^{2}A_{\mathrm{eff}}\frac{4\pi}{\lambda^{2}}G_{\mathrm{u}}S_{11}^{2}\left|\sum_{k=1}^{K}\frac{\sqrt{F_{\mathrm{f},k}}}{r'_{p,k}}\right|^{2}}.\tag{6}$$

Here, G_{f} is the gain of the reference antenna, and A_{eff} is the effective aperture of each RIS unit cell. The gain of the unit cell is denoted by G_{u}, and S_{11} is the reflection coefficient of the RIS surface due to the implemented structures and materials. The term $F_{\mathrm{f},k}$ is a normalized power radiation function between the reference antenna and each unit cell. Then, the RIS gain based on (5) is given by (7) with η showing the radiation efficiency. The observation range is set to be $\theta_{\mathrm{o}}\in[-\pi/2,\pi/2]$ and $\phi_{\mathrm{o}}\in[0,\pi]$, neglecting the power radiating to the backside of the RIS.

C. Received Signal and Link Budget

As depicted in Fig. 1(a), and based on the general RIS beamforming equation in (4), by setting $\theta=\theta_{\mathrm{Tx}}$, $\phi=\phi_{\mathrm{Tx}}$, and $p=p_1$, the unit cell phase shift at Tx RIS after the quantization $\varphi_{\mathrm{Tx},k}(\theta_{\mathrm{Tx}},\phi_{\mathrm{Tx}})$ is derived, yielding the beamforming matrix $\boldsymbol{\Phi}_{\mathrm{Tx}}$. Following the same logic, by setting $\theta=\theta_{\mathrm{Rx}}$, $\phi=\phi_{\mathrm{Rx}}$, and $p=p_4$, the Rx beamforming matrix $\boldsymbol{\Phi}_{\mathrm{Rx}}$ is obtained. Now, considering the RISs with the aforementioned beamforming design, the RIS-JCAS channel coefficient for sensing becomes

$$\begin{aligned}h_{\mathrm{rad,RIS}}(\theta_{p_2},\theta_{p_3},\phi_{p_2},\phi_{p_3},\theta_{\mathrm{Tx}},\theta_{\mathrm{Rx}},\phi_{\mathrm{Tx}},\phi_{\mathrm{Rx}})=\\\boldsymbol{h}_{p_4}\boldsymbol{\Phi}_{\mathrm{Rx}}\boldsymbol{h}_{p_3}^{T}\boldsymbol{h}_{p_2}\boldsymbol{\Phi}_{\mathrm{Tx}}\boldsymbol{h}_{p_1}^{T}.\end{aligned}\tag{8}$$

In comparison to (2), the distance phases are eliminated by $\varphi_{\mathrm{dis}}(r_{p,k})$ in (4), therefore the $r_{p,k}$ terms are neglected. New variables are added based on the beamforming directions at the Tx and Rx RISs. If any signal processing estimates the channel properly, which makes both Tx and Rx RISs beamforming to the UE direction, yielding $\theta_{p_2}=\theta_{\mathrm{Tx}}$, $\phi_{p_2}=\phi_{\mathrm{Tx}}$, $\theta_{p_3}=\theta_{\mathrm{Rx}}$, and $\phi_{p_3}=\theta_{\mathrm{Rx}}$ as depicted beamforming pattern in Fig. 1(a), the best system performance is achieved. For the next step, by transferring the RIS channel coefficient to a time-domain expression $h_{\mathrm{rad,RIS}}\rightarrow\alpha_{\mathrm{rad}}\delta(t-\tau_{\mathrm{rad}})$, and combining it with the transmit signal $x(t)$, the continuous time-domain baseband (BB) received signal for sensing is

$$\begin{aligned}y_{\mathrm{rad}}(t)=\alpha_{\mathrm{rad}}x(t-\tau_{\mathrm{rad}})e^{j2\pi f_{\mathrm{rad}}t}\\+\sum_{s=1}^{S_{\mathrm{rad}}}\alpha_{\mathrm{rad,s}}x(t-\tau_{\mathrm{rad,s}})e^{j2\pi f_{\mathrm{rad,s}}t}+n_{\mathrm{Rx}}(t).\end{aligned}\tag{9}$$

In this equation, synchronization offsets do not exist due to the fact of monostatic radar, and the mutual coupling between the Tx and Rx antennas is omitted for the sake of simplicity. The term $\tau_{\mathrm{rad}}=\sum_p\tau_p$ is the total signal delay through the four channels in (8) to derive the UE distance information, and f_{rad} is the Doppler shift to derive the UE velocity information with radar signal processing. The second part of the equation also considers the possibility of a total number of secondary paths, S_{rad}. They could be caused by the other possible objectives in the environment, which also reflect distinguishable power to the Rx due to the imperfection of the RIS beamforming, including sidelobes, quantization errors, beam steering, etc. The additional noise term is denoted by $n_{\mathrm{Rx}}(t)$. The parameter α_{rad} is a total attenuation factor through the channels in (8), which can be expressed as in (11), with $G_{\mathrm{Tx,RIS}}$ and $G_{\mathrm{Rx,RIS}}$ being the Tx and Rx RIS gain following the expression in (7), by setting the beamforming angles to $\theta=\theta_{\mathrm{Tx}}$ and θ_{Rx}, $\phi=\phi_{\mathrm{Tx}}$ and ϕ_{Rx}, then observing to the UE direction $\theta_{\mathrm{o}}=\theta_{p_2}$ and θ_{p_3}, $\phi_{\mathrm{o}}=\phi_{p_2}$ and ϕ_{p_3}. The term σ_{UE} is the radar cross section (RCS) of the UE. Therefore, the radar image SNR via the RIS-assisted channel following [9] is

$$SNR_{\mathrm{rad}}=\frac{\alpha_{\mathrm{rad}}^{2}G_{\mathrm{p}}}{k_{\mathrm{B}}TB_{\mathrm{rad}}F_{\mathrm{Rx}}}.\tag{10}$$

Here, G_{p} is the radar signal processing gain depending on the modulation scheme, which will be introduced in Section IV. k_{B} is the Boltzmann constant, T is the standard room temperature in Kelvin, B_{rad} is the radar signal bandwidth, and F_{Rx} is the overall Rx noise figure.

For the communication channel, only the Tx RIS will be used, therefore leading to the channel coefficients as

$$h_{\mathrm{com,RIS}}(\theta_{p_2},\phi_{p_2},\theta_{\mathrm{Tx}},\phi_{\mathrm{Tx}})=\boldsymbol{h}_{p_2}\boldsymbol{\Phi}_{\mathrm{Tx}}\boldsymbol{h}_{p_1}^{T}.\tag{12}$$

Similar to the derivation of (9), the continuous communication BB received signal assuming perfect synchronization is

$$y_{\mathrm{com}}(t)=\alpha_{\mathrm{com}}x(t-\tau_{\mathrm{com}})+\sum_{s=1}^{S_{\mathrm{com}}}\alpha_{\mathrm{com,s}}x(t-\tau_{\mathrm{com,s}})+n_{\mathrm{UE}}(t)\tag{13}$$

having a main path with propagation delay τ_{com} and secondary paths with delay $\tau_{\mathrm{com,s}}$. The noise term is considered at the UE with $n_{\mathrm{UE}}(t)$. The communication attenuation factor α_{com} can be expressed as

$$\alpha_{\mathrm{com}}=\sqrt{\frac{G_{\mathrm{Tx,RIS}}(\theta_{\mathrm{Tx}},\phi_{\mathrm{Tx}},\theta_{p_2},\phi_{p_2})\lambda^{2}G_{\mathrm{UE}}}{(4\pi r_{p_2})^{2}}}.\tag{14}$$

$$\alpha_{\mathrm{rad}} = \sqrt{\frac{G_{\mathrm{Tx,RIS}}(\theta_{\mathrm{Tx}}, \phi_{\mathrm{Tx}}, \theta_{p_2}, \phi_{p_2}) G_{\mathrm{Rx,RIS}}(\theta_{\mathrm{Rx}}, \phi_{\mathrm{Rx}}, \theta_{p_3}, \phi_{p_3}) \lambda^2 \sigma_{\mathrm{UE}}}{(4\pi)^3 (r_{p_2} r_{p_3})^2}}. \tag{11}$$

In comparison to (11), the UE RCS is replaced by the UE antenna gain G_{UE}. In the end, the communication signal SNR is given by

$$SNR_{\mathrm{com}} = \frac{\alpha_{\mathrm{com}}^2}{k_{\mathrm{B}} T B_{\mathrm{com}} F_{\mathrm{UE}}}, \tag{15}$$

with the communication signal bandwidth B_{com} and the noise figure at UE F_{UE}.

III. RIS-JCAS User Detection Algorithm

Based on the last section, it is obvious that the beamforming directions of the Tx and Rx RISs are the dominant factors in the radar and communication SNR from (10) and (15) since they directly influence the RIS gain in (7) while observing the UE direction. Also, the two spherical angle directions of the UE are important goals for 4D sensing besides range and velocity. Therefore, it is necessary to detect the DoD from the Tx RIS to the UE and the DoA from the UE to the Rx RIS. As discussed in [16], [32], due to the physical properties of RIS, conventional solutions to derive the channel state information via each RIS unit cell are hard to realize or impossible. Although the idea to use the orthogonal training matrix in [33] has been proved in [23], the complexity increases linearly with the number of unit cells, and it also needs very high SNR to ensure the computation accuracy, which is challenging for wireless signal propagations at mmWave frequencies. Fortunately, in comparison to the rich scattering characteristic for wireless propagations at lower frequencies, the behaviour at mmWave frequencies has angular sparse channel properties, with its mathematical model discussed in [34]. In other words, due to the high losses via the reflection and diffraction paths at mmWave frequencies, they are usually much weaker than the dominant LoS path. This is not only inspiring the utilization of RISs to provide qualified reflection paths but also validating the angle-dependent beam steering solution to efficiently derive the major DoD/DoA with minor distortion from other paths. Therefore, it is well accepted that beam training is the key to the solution, with the single RIS case studied in [15]. In this article, the proposed RIS-JCAS system in Fig. 1(a) needs the implementation of two RISs and the 2D beamforming direction. It is proposed in [35] that beam training on one side while using an omni pattern on the other side could be an option. This doubles the measurement effort, along with the possibility of target loss due to the low gain of the omni pattern. The situation could be even worse for RIS when each unit cell has low phase resolution, which can only generate a poorly qualified omni pattern with its gain strongly angle-dependent, as shown in [10]. This further increases the risk of target loss and is even more critical for JCAS because a target at any "gain valley" out of the dynamic range might be neglected. To solve this, RIS beams with higher directionality could be used on both sides, but the measurement effort would be at an exponential level. To overcome the challenges above, an efficient and accurate algorithm to realize RIS-JCAS sensing and channel estimation is proposed.

A. Joint RIS-JCAS Beam Training

For a conventional monostatic JCAS system, the Tx and Rx antennas are placed next to each other at the BS, which makes the forward and backward channels nearly overlap with each other. Although this stands true for the BS Tx and Rx antennas in Fig. 1(a), the main task in the RIS-JCAS system is sensing the channel between RISs and UE, yielding $\boldsymbol{h}_{p_2}$ and $\boldsymbol{h}_{p_3}$, while the channels $\boldsymbol{h}_{p_1}$ and $\boldsymbol{h}_{p_4}$ between the stationary BS and RISs previously known. To increase the possibility of sensing the UE, the two RISs should be located close to each other to avoid the unnecessary constraint that the UE must be in an area that is visible to two significantly spatially separated RISs. However, because a RIS contains a massive number of unit cells, it usually has a relatively large size. In addition, to avoid mutual coupling between the Tx and Rx RIS and let them serve the Tx and Rx as independently as possible to optimize the beamforming quality, it is also preferred to allocate the RIS with proper distances between them. As a consequence, the two RISs are defined to be located on the same plane (xz plane in Fig. 1(b)), indicating the practical scenario that they are both attached to the same building sidewall. As a consequence, this leads to a quasi-monostatic RIS-JCAS system with the distance D between the RIS phase centers.

In principle, the existence of D will bring a considerable difference between $\boldsymbol{h}_{p_2}$ and $\boldsymbol{h}_{p_3}$, yielding $\theta_{p_2} \neq \theta_{p_3}$ and $\phi_{p_2} \neq \phi_{p_3}$, which requires separate beamforming matrices $\boldsymbol{\Phi}_{\mathrm{Tx}}$ and $\boldsymbol{\Phi}_{\mathrm{Rx}}$ derivation with high complexity. As a solution, a joint beam training process is proposed in this article by setting $\boldsymbol{\Phi}_{\mathrm{Tx}} = \boldsymbol{\Phi}_{\mathrm{Rx}}$, which significantly reduces the beam training measurement steps. To achieve this, two possible methods are described below:

1) High-directional beam exhaustive search: Firstly, the 2D RIS beamforming range with θ_{s} to θ_{e} and ϕ_{s} to ϕ_{e} as the starting to ending angle along both dimensions are defined. The angle resolution is g_{n}, yielding $\boldsymbol{\theta}_{\mathbf{n}} = \{\theta_{\mathrm{s}}, \theta_{\mathrm{s}} + g_{\mathrm{n}}, ..., \theta_{\mathrm{s}} + g_{\mathrm{n}}(n_\theta - 1), ..., \theta_{\mathrm{s}} + g_{\mathrm{n}}(N_\theta - 1)\}$ and $\boldsymbol{\phi}_{\mathrm{n}} = \{\phi_{\mathrm{s}}, \phi_{\mathrm{s}} + g_{\mathrm{n}}, ..., \phi_{\mathrm{s}} + g_{\mathrm{n}}(n_\phi - 1), ..., \phi_{\mathrm{s}} + g_{\mathrm{n}}(N_\phi - 1)\}$ showing the 2D beamforming candidates. By examining them while keeping $\boldsymbol{\Phi}_{\mathrm{Tx}} = \boldsymbol{\Phi}_{\mathrm{Rx}}$, the best beamforming candidate $\theta_{\mathrm{b}}, \phi_{\mathrm{b}}$ is determined by the maximized radar SNR in (10), which is effectively the RIS gain part in (11), expressed as (16).

2) Flat-top beam hierarchical search: The efficiency of the aforementioned exhaustive search method can be further improved with the flat-top beam, which covers a wider range than a RIS high-directional beam. To realize the flat-top beam stated in [36], a RIS can generate multiple subbeams fairly close to each other, as proved in [37]. Therefore, the beam

$$\theta_{\mathrm{b}}, \phi_{\mathrm{b}} = \underset{\theta_{\mathrm{Tx}}=\theta_{\mathrm{Rx}}\in\boldsymbol{\theta}_{\mathbf{n}}, \phi_{\mathrm{Tx}}=\phi_{\mathrm{Rx}}\in\boldsymbol{\phi}_{\mathbf{n}}}{\operatorname{argmax}} SNR_{\mathrm{rad}} \Rightarrow G_{\mathrm{Tx,RIS}}(\theta_{\mathrm{Tx}}, \phi_{\mathrm{Tx}}, \theta_{p_2}, \phi_{p_2}) G_{\mathrm{Rx,RIS}}(\theta_{\mathrm{Rx}}, \phi_{\mathrm{Rx}}, \theta_{p_3}, \phi_{p_3}) \tag{16}$$

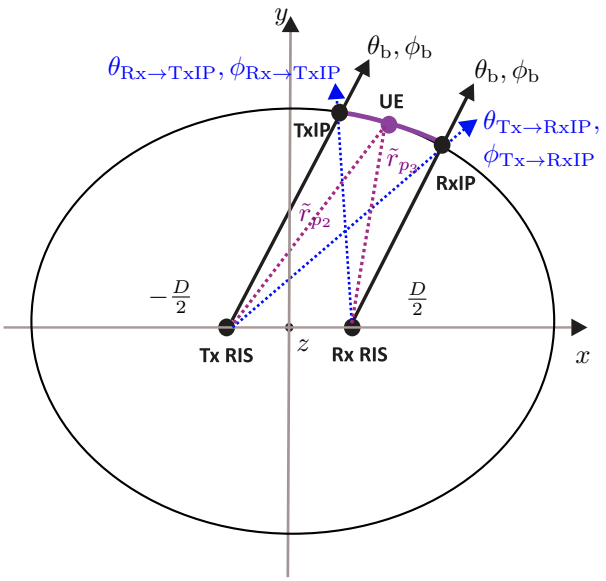

Fig. 2. The top view of the ellipsoid formulated by the sensing estimation based on (18). The Tx RIS is centered at $(-D/2, 0, 0)$, and the Rx RIS is centered at $(D/2, 0, 0)$. The angles $\theta_{\mathrm{b}}, \phi_{\mathrm{b}}$ indicate the beamforming direction derived from (16). The dashed blue lines show the margin angles from the Tx RIS and Rx RIS point of view derived from (19).

steering part $\psi_{\mathrm{ste}}(k, \theta, \phi)$ in (4) will be changed to

$$\psi_{\mathrm{ste,f}}(k, \theta, \phi) = \angle\Big(\sum_{\mathrm{b_f}=1}^{B_{\mathrm{f}}} e^{j\psi_{\mathrm{ste}}(k, \theta_{\mathrm{b_f}}, \phi_{\mathrm{b_f}})}\Big) \tag{17}$$

for the generation of flat-top beams centralized at θ, ϕ, with B_{f} high-directional beams to $\theta_{\mathrm{b_f}}, \phi_{\mathrm{b_f}}$ directions chosen properly. As a consequence, the flat-top beam leads to a change of the angle resolution g_{n} in the high-directional beam case to $g_{\mathrm{f},\theta}$ and $g_{\mathrm{f},\phi}$, yielding the flat-top beamforming candidates $\boldsymbol{\theta}_{\mathrm{f}} = \{\theta_{\mathrm{s}}, \theta_{\mathrm{s}}+g_{\mathrm{f},\theta}, ..., \theta_{\mathrm{s}}+g_{\mathrm{f},\theta}(n_{\mathrm{f},\theta}-1), ..., \theta_{\mathrm{s}}+g_{\mathrm{f},\theta}(N_{\mathrm{f},\theta}-1)\}$ and $\boldsymbol{\phi}_{\mathrm{f}} = \{\phi_{\mathrm{s}}, \phi_{\mathrm{s}} + g_{\mathrm{f},\phi}, ..., \phi_{\mathrm{s}} + g_{\mathrm{f},\phi}(n_{\mathrm{f},\theta} - 1), ..., \phi_{\mathrm{s}} + g_{\mathrm{f},\phi}(N_{\mathrm{f},\phi}-1)\}$. Then, by computing (16) using $\boldsymbol{\theta}_{\mathrm{f}}$ and $\boldsymbol{\phi}_{\mathrm{f}}$, the altered result provides the best flat-top beam. This procedure can be repeated a few times with a gradually reduced flat-top beam width, as mentioned in [35]. Afterwards, a small range of exhaustive searches using high-direction beams with angle resolution g_{n} within the last flat-top beamforming coverage is implemented using (16) to finalize the $\theta_{\mathrm{b}}, \phi_{\mathrm{b}}$. This method will decrease the measurement effort depending on how broad the flat top beams are, as stated in [35]. However, it also decreases SNR_{rad} since the RIS gain in (7) will be scattered to a wide range rather than the precise DoD/DoA between the RISs and UE, which will be considered and mitigated in the JCAS signal processing design in Section IV.

B. Beam Fine-Tuning

The beamforming direction $\theta_{\mathrm{b}}, \phi_{\mathrm{b}}$ is a sub-optimum solution regardless of the difference between θ_{p_2}, ϕ_{p_2} and θ_{p_3}, ϕ_{p_3}. This is sufficient to capture a fair amount of power reflected from the UE and suppress the secondary paths to obtain the UE range and velocity estimation based on the received signal (9) using typical radar signal processing. However, the angle information for the 4D sensing is not accurate, which will lead to unclear UE localization and communication link budget degradation. Therefore, a fine-tuning method is required to further update the optimum beamforming direction for Tx and Rx RIS separately. To achieve this, a fine-tuning range needs to be firstly defined based on $\theta_{\mathrm{b}}, \phi_{\mathrm{b}}$. Under the previously mentioned scenario definition that both RISs are on the same plane, their phase centers can be depicted on the same line, for example, on the x-axis of Fig. 2. Now, based on the range R estimated from the propagation delay in (9) with radar signal processing, the effective distance of Tx RIS $\to$ UE $\to$ RX RIS is $2r_{\mathrm{RIS}} = 2R - r_{p_1} - r_{p_4} = \tilde{r}_{p_2} + \tilde{r}_{p_3}$. The factor of 2 is introduced by the round-trip propagation. Based on the ellipsoid theorem, considering the distance D between RISs, they exactly formulate a 3D ellipsoid centralized in the middle of the two RISs as

$$\frac{x^2}{r_{\mathrm{RIS}}^2} + \frac{y^2}{r_{\mathrm{RIS}}^2 - (\frac{D}{2})^2} + \frac{z^2}{r_{\mathrm{RIS}}^2 - (\frac{D}{2})^2} = 1. \tag{18}$$

For simple vision, a top view to the xy plane is depicted in Fig. 2. The denominator for x^2 depends on $r_{\mathrm{RIS}} = (\tilde{r}_{p_2} + \tilde{r}_{p_3})/2$ given by the dashed purple curves, with r_{RIS} the semi-major along x-axis. The denominator for y^2 can be calculated using the Pythagorean theorem. The denominator for z^2 is the same as y^2 while fixing the position of the RISs and rotating the 2D ellipse to the xz plane. Besides the ellipsoid, the reference lines starting from the Tx RIS and Rx RIS with beamforming directions can be defined as

$$\begin{aligned} \mathrm{TxRIS}: \ & y_{\mathrm{Tx}} = \frac{(x_{\mathrm{Tx}} + D/2)}{\tan\theta_{\mathrm{Tx}} \sin\phi_{\mathrm{Tx}}}, z_{\mathrm{Tx}} = \frac{(x_{\mathrm{Tx}} + D/2)}{\tan\phi_{\mathrm{Tx}}}; \\ \mathrm{RxRIS}: \ & y_{\mathrm{Rx}} = \frac{(x_{\mathrm{Rx}} - D/2)}{\tan\theta_{\mathrm{Rx}} \sin\phi_{\mathrm{Tx}}}, z_{\mathrm{Rx}} = \frac{(x_{\mathrm{Rx}} - D/2)}{\tan\phi_{\mathrm{Rx}}}. \end{aligned} \tag{19}$$

By setting $\theta_{\mathrm{Rx}} = \theta_{\mathrm{Tx}} = \theta_{\mathrm{b}}$ and $\phi_{\mathrm{Rx}} = \phi_{\mathrm{Tx}} = \phi_{\mathrm{b}}$, the interception points with the ellipsoid at TxIP and RxIP in Fig. 2 can be derived, which formulates the curve C(TxIP, RxIP) indicating the range where the UE is located. Afterwards, by evaluating the angles along C(TxIP, RxIP) from Tx and Rx RIS separately, the angle set considering discrete quantization is

$$\begin{aligned} \mathrm{TxRIS}: & \begin{cases} \boldsymbol{\theta}_{\mathrm{Tx,tune}} &= [\theta_{\mathrm{b}} : g_{\mathrm{r}} : \theta_{\mathrm{Tx}\to\mathrm{RxIP}}]; \\ \boldsymbol{\phi}_{\mathrm{Tx,tune}} &= [\phi_{\mathrm{b}} : g_{\mathrm{r}} : \phi_{\mathrm{Tx}\to\mathrm{RxIP}}]; \end{cases} \\ \mathrm{RxRIS}: & \begin{cases} \boldsymbol{\theta}_{\mathrm{Rx,tune}} &= [\theta_{\mathrm{Rx}\to\mathrm{TxIP}} : g_{\mathrm{r}} : \theta_{\mathrm{b}}]; \\ \boldsymbol{\phi}_{\mathrm{Rx,tune}} &= [\phi_{\mathrm{Rx}\to\mathrm{TxIP}} : g_{\mathrm{r}} : \phi_{\mathrm{b}}]; \end{cases} \end{aligned} \tag{20}$$

The margin angles $\theta_{\mathrm{Rx}\to\mathrm{TxIP}}, \phi_{\mathrm{Rx}\to\mathrm{TxIP}}$ could be derived by inputting the coordinates of TxIP into the RxRIS equation in (19). Following the same logic, other margin angles $\theta_{\mathrm{Tx}\to\mathrm{RxIP}}, \phi_{\mathrm{Tx}\to\mathrm{RxIP}}$ can be also obtained. By iterating the angle combinations in (20) to trace C(TxIP, RxIP), there will be one of the Tx and Rx RIS beamforming angle combinations

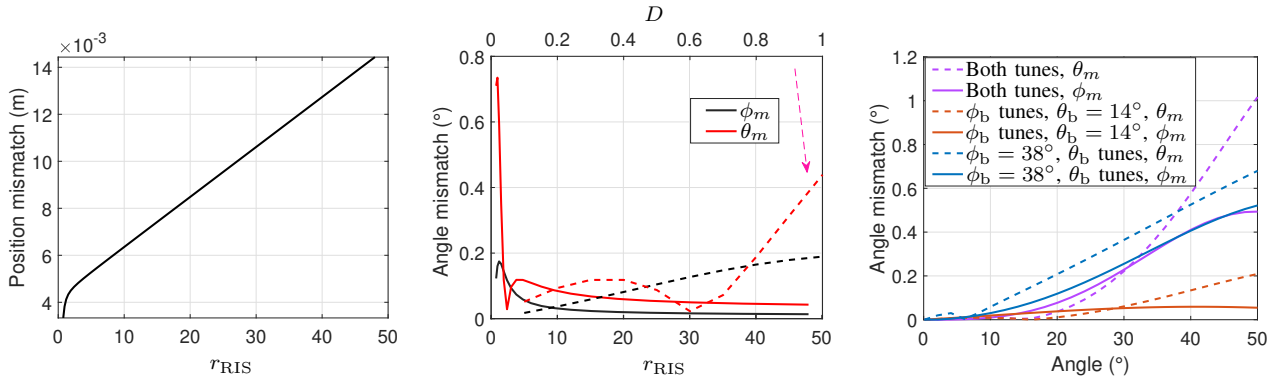

Fig. 3. Simulation analysis of the proposed fine-tuning algorithm accuracy. (a) Position mismatch vs. propagation distance. (b) Angle mismatches θ_m (red), ϕ_m (black) vs. propagation distance (solid with bottom axis) and D (dashed with upper axis). (c) Angle mismatches θ_m (solid), ϕ_m (dashed) vs. beamforming angle θ_{b}, ϕ_{b} from (16), for θ_{b}, ϕ_{b} both tuning (purple); θ_{b} tuning, $\phi_{\mathrm{b}} = 38°$ fixed (orange); $\theta_{\mathrm{b}} = 14°$ fixed, ϕ_{b} tuning (blue).

closest to the actual UE position yielding the best system performance, for the optimum case, directly formulating the purple lines in (19) crossing at the UE in Fig. 2. As the conventional solution, an exhaustive search using high-directional beams could be operated to examine all the possibilities in (20) considering a quantization with RIS beamforming angle resolution $g_{\mathrm{n}} = g_{\mathrm{r}}$. The results can deliver the best angle combination for further JCAS signal processing, but the exact UE position is still missing because the processing has to follow the limited RIS beamforming angle resolution, which will probably not offer any 3D crossing point of the lines in (19). Therefore, a least-square beam fine-tuning method is proposed in this article to derive the RIS angle combination as well as the 3D UE position in the coordinates without any additional measurement effort.

The first step of the method is finding a convincible axis, along which there is less likely to have UE position mismatch, while z or y-axis can be chosen based on the coordinate in Fig. 2 since the only position difference of the RIS is the distance D along x-axis. By choosing the z axis as an example for the following method description, the next step is to find a computation plane which is perpendicular to the convincible axis, yielding the xy-plane. Then, the mapping of the two reference lines can be taken from the y and x relationship part in (19) with $\theta_{\mathrm{Rx}} \in \boldsymbol{\theta}_{\mathrm{Rx,tune}}, \phi_{\mathrm{Rx}} \in \boldsymbol{\phi}_{\mathrm{Rx,tune}}$ and $\theta_{\mathrm{Tx}} \in \boldsymbol{\theta}_{\mathrm{Tx,tune}}, \phi_{\mathrm{Tx}} \in \boldsymbol{\phi}_{\mathrm{Tx,tune}}$ from (20). For each angle combination along C(TxIP, RxIP), a 2D crossing point (CP) that satisfies (19) on the computation plane with $x_{\mathrm{cp}} = x_{\mathrm{Tx}} = x_{\mathrm{Rx}}$ and $y_{\mathrm{cp}} = y_{\mathrm{Tx}} = y_{\mathrm{Rx}}$ can be derived. Collecting all the 2D CPs and combining them with the convincible axis value $z = z_{\mathrm{c}}$ will formulate a 3D CP at $(x_{\mathrm{cp}}, y_{\mathrm{cp}}, z_{\mathrm{c}})$, with all of them lead to a set $\boldsymbol{CP}$. Then, by computing the distance of Tx RIS $\rightarrow (x_{\mathrm{cp}}, y_{\mathrm{cp}}, z_{\mathrm{c}}) \rightarrow$ Rx RIS, and comparing the value with the estimated distance $2r_{\mathrm{RIS}}$, the one having the minimum difference is chosen as the estimated UE position $(x_{\mathrm{UE}}, y_{\mathrm{UE}}, z_{\mathrm{UE}})$, which corresponds to a pair of angle in (20), leading to the derivation of DoD/DoA for the Tx/Rx RIS given in (21).

The choice of $z = z_{\mathrm{c}}$ dominates the performance and needs to be further discussed. In the proposed method, $z_{\mathrm{c}} = \frac{z_{\mathrm{TxIP}} + z_{\mathrm{RxIP}}}{2} \approx z_{\mathrm{TxIP}} \approx z_{\mathrm{RxIP}}$ is used to ensure a reduced complexity looking for a proper CP on a 2D plane in Fig. 2. In Fig. 3, the accuracy of this idea is proved with simulations for the RIS-JCAS system under different geometries, represented by the parameters including the spatial distance between the Tx and Rx RIS D, the target distance derived from radar sensing r_{RIS}, and the sub-optimum angle determined from (16). Please notice that the values of these parameters are independent of any specific system settings to realize a general analysis of the proposed system in different objective conditions. Firstly, the r_{RIS} increases from $0.33\,\mathrm{m}$ to $48\,\mathrm{m}$ with fixed choices of $\theta_{\mathrm{b}} = 14°, \phi_{\mathrm{b}} = 38°, D = 0.3\,\mathrm{m}$ in Fig. 3(a). This figure shows the mismatch between the approximated position z_{c} and the estimated positions z_{TxIP} and z_{RxIP}. It is visible that the position mismatch increases in magnitude with increasing r_{RIS}, but mainly due to the geometric extension. Nevertheless, this mismatch is kept at a minimal relative value, for example, when r_{RIS} reaches $48\,\mathrm{m}$, the mismatch is only $0.014\,\mathrm{m}$, which is neglectable since this is mostly beyond the normal radar estimation resolution. Besides the position mismatch, another important standard to evaluate accuracy is the angle mismatch from the RIS point of view. By observing solid curves in Fig. 3(b), it could be seen that the 2D angle mismatch behaves similarly to the position mismatch: when the UE is farther away from the RISs, the angular mismatch is smaller. This is a great observation, since for longer propagation distances, more RIS unit cells are desired to compensate for the stronger FSPL, which leads to a narrower beam. This will require higher algorithmic accuracy, and the decreasing angle mismatch with increasing distance exactly fulfills the condition. Even with a small r_{RIS}, the angle mismatch does not exceed $0.8°$, which is less than half of the prototype RIS angle resolution of $2°$ in [15]. In addition, when the UE is close to the RISs, the mismatch in practice is also less important since the UE will easily capture high power due to the reduced FSPL. Besides the aforementioned general trend, there are some fluctuations for smaller r_{RIS} since the ratio of D/r_{RIS} is larger, which means the distance between the two RIS plays a greater role. To analyze the influence of D, the dashed curves in Fig. 3(b) show the angle mismatches

with $\theta_{\mathrm{b}} = 14°, \phi_{\mathrm{b}} = 38°$ and a changing D, which have fairly small values for both 2D angles. The distance D is simulated up to $1\,\mathrm{m}$ since it is mentioned in Section III that the two RISs are not located in significantly different positions for the proposed system. In Fig. 3(c), r_{RIS} is fixed to $4.65\,\mathrm{m}$ and D = $0.3\,\mathrm{m}$ to observe the angle mismatch for the angular range of θ_{b} and ϕ_{b} determined from (16) in the range of $-50°$ to $50°$. Since the ellipsoid in Fig. 2 has symmetrical properties, only half of the angle range from 0 to $50°$ is shown. It could be visible that the angle mismatch increases when UE is at a larger tilting angle. Also, when a smaller θ_{b} is used than ϕ_{b}, the angle mismatch increases slower. These observations are because the absolute distance in a Cartesian coordinate varies more for a larger tilting angle. When both θ_{b} and ϕ_{b} tune, the largest mismatch reaches $\theta_m = 1°$ and $\phi_m = 0.68°$ at $\theta_{\mathrm{b}} = \phi_{\mathrm{b}} = 50°$, which are still under the $2°$ tolerance range in [15]. The angle θ has more mismatches than the angle ϕ in a solid curve since it has more contributions in the z-axis based on the coordinates in Fig. 1(b) and conditions in (19).

C. Algorithm Overview

The entire algorithmic process is presented in Algorithm 1 as a brief conclusion to the aforementioned subsections. In general, by inputting the system design parameters, the joint beam training is operated first, which provides the sub-optimum RIS angles $\theta_{\mathrm{b}}, \boldsymbol{\phi}_b$ as well as UE range and velocity estimation. The final UE position and the DoD/DoA from the RIS point of view are derived by the fine-tuning algorithm.

Algorithm 1: JCAS UE detection algorithm

Input: d, M_{Tx}, N_{Tx}, M_{Rx}, N_{Rx}, D, g_{r}
if ***Exhaustive search*** **then**
  Input:$\boldsymbol{\theta}_{\mathbf{n}}$,$\boldsymbol{\phi}_n$
end
if ***Hierachical codebook*** **then**
  Input:$\boldsymbol{\theta}_{\mathrm{f}}$,$\boldsymbol{\phi}_{\mathrm{f}}$,$g_{\mathrm{n}}$,$g_f$
  while $g_{\mathrm{n}} < g_f$ **do**
    Update $\boldsymbol{\theta}_{\mathrm{f}}, \boldsymbol{\phi}_{\mathrm{f}}, g_f$ with (16)
  end
end
Finalize $\theta_{\mathrm{b}}, \boldsymbol{\phi}_b$ with (16)
Output:R, r_{RIS}, UE velocity
Derive the JCAS ellipsoid based on (18)
Derive TxIP and RxIP based on (18) and (19)
Derive angle tuning range based on (20) along C(TxIP, RxIP).
Compute CPs based on (19)
Finalize UE position based on (21)
Output:$\theta_{\mathrm{Tx}}, \phi_{\mathrm{Tx}}, \theta_{\mathrm{Rx}}, \phi_{\mathrm{Rx}}, x_{\mathrm{UE}}, y_{\mathrm{UE}}, z_{\mathrm{UE}}$

IV. RIS-JCAS Signal Processing

The signal processing chain of the RIS-JCAS system is depicted in Fig. 4 and can be mainly divided into Tx and Rx BS signal processing, as well as UE signal processing. The proposed RIS-JCAS system and signal processing model can be exploited as the distributed networks following the concept in [38]. The operational flow contains communication, RIS signal processing, and wireless sensing, which fulfil the trend of the further wireless network. This section focuses mainly on the difference that RIS brings to the RIS-JCAS system, while detailed information on the JCAS processing itself can be found in [4], [9].

A. BS Tx and Rx Signal Processing

Aiming to comply with current and future wireless communication standards, OFDM is adopted as the main modulation scheme for the RIS-JCAS system. While OFDM has the advantage of high spectrum efficiency, it suffers from high peak-to-average power ratio (PAPR), which may ultimately require a backoff of more than $10\,\mathrm{dB}$ from the saturation point of power amplifier (PA) to avoid non-linearities. This may significantly limit the sensing dynamic range of the RIS-JCAS system, which becomes particularly critical during the flat-top hierarchical search performed by the BS as described in Section III-A. As a solution, an OCDM frame with M_s^{OCDM} identical symbols is adopted for the flat-top beam search. Out of the N_c^{OCDM} subchirps in each symbol, only the first one is active, and discrete-Fresnel domain radar signal processing described in [4] is utilized. Regarding compliance with wireless communication standards, OCDM remains an attractive candidate modulation scheme due to its compatibility with OFDM as discussed in [39]. While other waveforms such as phase modulated continuous wave (PMCW) are also considered for JCAS [9], they are mainly adopted in radar-centric applications where low data rates and limited waveform flexibility are needed, therefore not suitable for communication-centric JCAS applications such as the one in this article.. The aforementioned OCDM waveform, however, yields significantly lower PAPR than OFDM due to a similar effect on tone reservation. Additionally, it does not require cyclic prefix since all OCDM symbols within a frame are equal, which allows for transmitting a higher number of OCDM symbols within the same frame duration compared to the OFDM case and therefore yields higher radar processing gain $G_{\mathrm{p}}^{\mathrm{OCDM}} = N_c^{\mathrm{OCDM}} M_s^{\mathrm{OCDM}}$ in the ultimately obtained range-velocity radar images. Or, in another case, achieve the same processing gain using fewer symbols. It is worth highlighting that all the $N_c^{\mathrm{OCDM}} M_s^{\mathrm{OCDM}}$ samples in the OCDM frame contribute to the radar processing gain, which is not the case in OFDM-based JCAS systems since the samples used for cyclic prefix must be discarded before radar signal processing at the receiver [4]. These two effects combined serve as a countermeasure to the beamforming gain reduction experienced in the flat-top beam search, reducing or even fully compensating the experienced dynamic range reduction. After a rough target angle estimation is performed with the flat-top beam search stage of the hierarchical search,

$$(\theta_{\mathrm{Tx}}, \phi_{\mathrm{Tx}}, \theta_{\mathrm{Rx}}, \phi_{\mathrm{Rx}}, x_{\mathrm{UE}}, y_{\mathrm{UE}}, z_{\mathrm{UE}}) = \underset{x,y,z \in \boldsymbol{CP}}{\operatorname{argmin}} |2r_{\mathrm{RIS}} - \sqrt{(x+d/2)^2 + y^2 + z^2} - \sqrt{(x-d/2)^2 + y^2 + z^2}|. \tag{21}$$

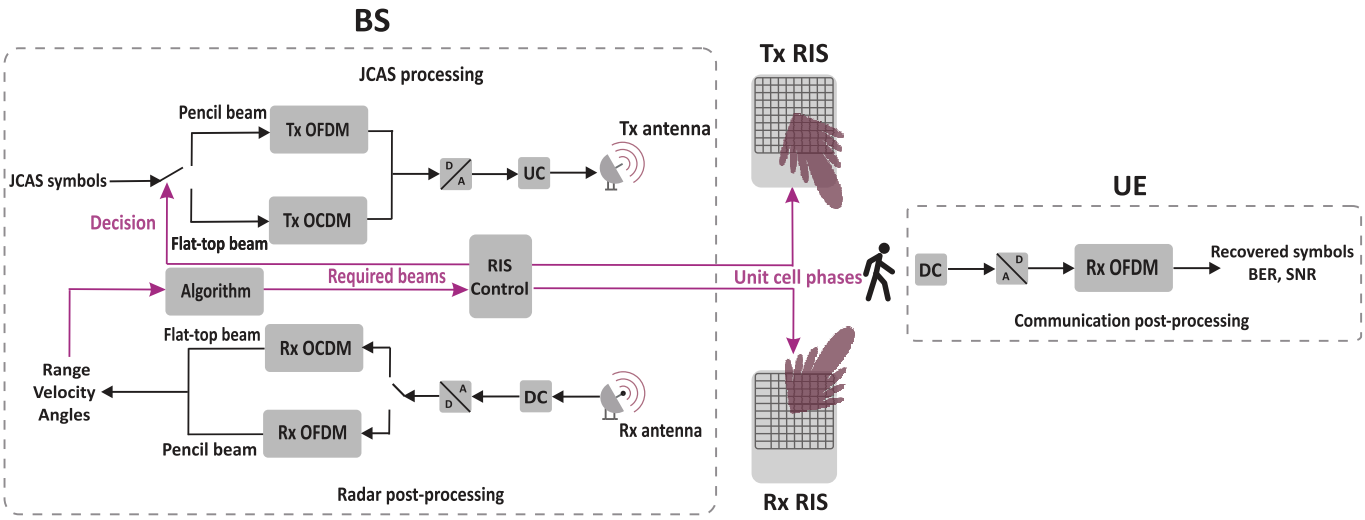

Fig. 4. Signal processing diagram for RIS-JCAS, considering the existence of digital to analog converters (DAC), analog to digital converter (ADC), frequency up/down conversions (UC/DC).

the BS of the RIS-JCAS switches its transmit waveform back to OFDM for the reduced-range exhaustive search, where high-directional beams are more likely to sufficiently cover potential targets/UEs even if not pointed at optimal directions, despite the dynamic range reduction due to the high PAPR in OFDM, enabling both radar sensing and communication. The adopted parameterization for OFDM includes a number M_s^{OFDM} of OFDM symbols within a frame, each with N_c^{OFDM} subcarriers and cyclic prefix length N_{cp}^{OFDM}, which results in a total number of samples $(N_c^{\mathrm{OFDM}} + N_{cp}^{\mathrm{OFDM}})M_s^{\mathrm{OFDM}}$ in the OFDM frame and a processing gain $G_{\mathrm{p}}^{\mathrm{OFDM}} = N_c^{\mathrm{OFDM}} M_s^{\mathrm{OFDM}}$ for the ultimately obtained range-velocity radar images. The detailed transmit processing chains based on the aforementioned OCDM and OFDM modulation schemes, as well as the achieved radar performance parameters such as range and velocity maximum unambiguous values and resolutions, are described in [4] and [9], respectively.

The block diagram for both described signal processing chains is depicted in Fig. 4, where the BS generates the JCAS Tx signal and only performs radar signal processing at the Rx side. It can be seen that OCDM and OFDM are chosen based on the decision from the RIS control center. The decision comes from the algorithm block operating Alg.1 according to the range, velocity, and angle information of the UE detected by the radar signal processing, which will define whether a flat-top beam search, a reduced-range exhaustive search, or communication using a determined high-directional beam will be performed. When high-directional beams are formed, the OFDM transmit processing chain is chosen, while its OCDM counterpart is selected for the flat-top beam. Simultaneously, the RIS control center also determines the phase states of the RIS unit cells based on the output of Alg.1. In practice, the control center should be constructed with the BS, while the control of the RISs can be realized with global positioning system (GPS) antennas or fiber Ethernet lines since both BS and RISs are attached to buildings.

B. UE Communication Signal Processing

As proposed in the system model from Fig. 1(a) and the algorithm in Section III, the BS will first sense the UE and then communicate with it using an OFDM waveform. Since the communication channel from (12) is actually a part of the radar channel (8), the system can reuse the sensing results directly for communication purposes, most importantly, the beamforming direction RIS $\theta_{\mathrm{Tx}}, \phi_{\mathrm{Tx}}$ derived from Algorithm 1 to maximize the SNR in (15). In addition, to recover the communication signal, pilot subcarriers are also required for the channel frequency response (CFR) estimation [40] and subsequent equalization, which does not affect the radar signal processing. The aforementioned steps require time, carrier frequency, and sampling frequency synchronization between the BS transmitter and UE receiver, which, e.g., can be achieved based on the use of additional preamble OFDM symbols as described in [40]. In this article, however, perfect synchronization is assumed for the sake of simplicity. After the aforementioned processing steps, the transmitted communication symbols by the BS can be efficiently recovered at UE. The obtained symbols can be further evaluated to compute the modulation error ratio (MER), bit error ratio (BER), or other metrics for communication performance analysis. In the considered scenario, the UE is assumed to solely operate as a communication receiver, having, therefore, no knowledge of the status of the BS RIS control center.

V. JCAS-RIS Measurement Setup

The system model in Fig. 1(a) and the signal processing in Fig. 4 are jointly realized by the experimental RIS-JCAS system in Fig. 5, which is placed in an anechoic chamber at KIT. The major device imitating the CCU at the BS is the laptop. It operates the digital parts of the Tx signal processing and the Rx radar signal processing. The laptop can upload signals to or download signals from a Xilinx FPGA-based Radio Frequency System on Chip (RFSoC), which realizes the conversion between the digital signal and the analog signal centralized at 1 GHz intermediate frequency (IF) with 1 GHz

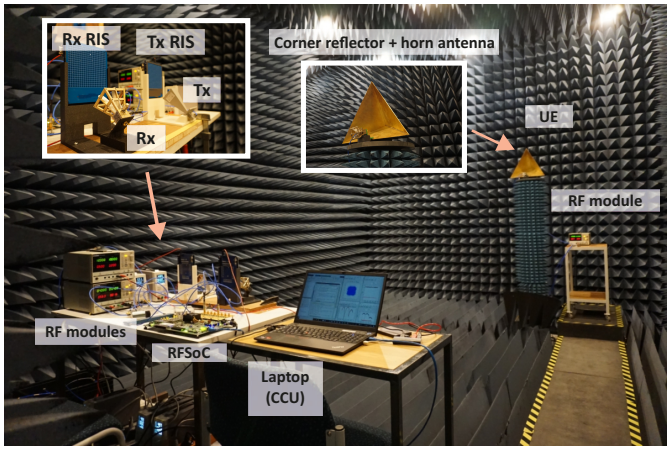

Fig. 5. The experimental RIS-JCAS system in this article.

bandwidth. In this case, synchronization between the Tx and Rx is not required due to the monostatic property. Afterwards, the conversion between the IF signal and the mmWave RF signal at the carrier frequency of $26.2\,\mathrm{GHz}$ is realized by the RF modules used in [15]. For each RIS, a horn antenna is used as the reference antenna, with a fixed geometric position. In this article, the experimental system uses the nearfield illuminated RIS case as a representation. Nevertheless, the channels for $\boldsymbol{h}_{p_1}$ and $\boldsymbol{h}_{p_4}$ in (8) are always previously known, so beamforming patterns $\boldsymbol{\Phi}_{\mathrm{Tx}}$ and $\boldsymbol{\Phi}_{\mathrm{Rx}}$ can be pre-designed with (4) using $26.2\,\mathrm{GHz}$ as the reference frequency for the entire band. These patterns are loaded onto the RIS control panel, which is further commanded by the laptop, therefore realizing the cooperative signal processing chain in Fig. 4. The RISs used in this article is the design from [12], which are PIN-diode-based designs with $M_{\mathrm{Tx}}\times N_{\mathrm{Tx}} = M_{\mathrm{Rx}}\times N_{\mathrm{Rx}} = 20\times 20$ units cells, yielding a $L = 1$ bit phase resolution. The UE is imitated by a corner reflector equipped with a horn antenna in Fig. 5 as a typical target representation for radar sensing experiments following [41]. To ease the hardware effort, the communication Rx signal processing is also realized by the laptop in this article. This measurement setup is chosen as a representation of the RIS-JCAS system, and the scenario can be altered to different applications previously studied in [23].

VI. Results Analysis

A. Parameter Settings

In the proof-of-concept measurements, flat-top beam search with OCDM signals is performed to find out in which angular sector the target/UE is located. Afterwards, an exhaustive search over a reduced angular range is performed with pencil beams and the OFDM waveform. This method refers to the parameters in Table I, while the measurements with other methods will be discussed accordingly later in this section. Overall, the observation area of interest is assumed to be covered by the angular range from $\theta_{\mathrm{s}} = 0^\circ$ to $\theta_{\mathrm{e}} = 30^\circ$, and $\phi_{\mathrm{s}} = 20^\circ$ to $\phi_{\mathrm{e}} = 46^\circ$. For the flat-top search, a total of 42 angular sectors with steps of $g_{\mathrm{f},\theta} = 10^\circ$ and $g_{\mathrm{f},\phi} = 2^\circ$ are scanned with OCDM. After the sector where the target/UE is located is identified, the aforementioned reduced exhaustive search is performed for 6 angular sectors, which are defined keeping the estimated ϕ angle from the flat-top search and sweeping the remaining θ range with a step of $g_{\mathrm{n}} = 2^\circ$. The detailed beam shaping ability of the utilized RIS can be found in [37]. The RIS beamforming for a broad-band multicarrier system is determined by the center frequency, based on the previous research. The study in [42] proves that the RIS unit cell phase determination can apply the maximum channel impulse response method with minor performance degradation. This method forces all the RIS unit cells to serve the strongest path, yielding the LoS DoA/DoD path between the RIS and Tx/Rx, which formulates a quasi-frequency flat channel that validates the unique RIS unit cell phases through all the subcarriers. It is also mentioned in [43], [44] that the RIS beamforming pattern does not differ much due to small frequency or phase mismatch, which stands true for the $1\,\mathrm{GHz}$ bandwidth centralized at $26.2\,\mathrm{GHz}$ in Table I. In addition, the phase and amplitude variants of the signals caused by the RIS design will be contained in the cascaded channel coefficients in (2) and (3), which can be treated subcarrier-wise for the radar sensing and communication signal recovery. The radio-frequency (RF) and OCDM/OFDM signal parameters listed in Table I are adopted. To define the parameters in this table, a speed of $2\,\mathrm{m/s}$ was assumed for the target/UE, which is higher than the average speed of pedestrians defined in [45]. With this number, the OFDM symbol is decided to be 1024, which leads to a processing gain of 63.22dB. For OCDM, considering the 7.15dB gain due to a normalized PAPR computed in [4] and the 4dB beam broadening loss measured in [37], 60.21dB processing gain is sufficient to realize the same performance as OFDM, yielding a halved utilized symbol of 512. By transferring the symbol length to frame duration, this leads to the measurement time of flat-top beam hierarchical search with OCDM ($44.04\,\mathrm{ms}$) and high-directional exhaustive beam search with OFDM ($15.73\,\mathrm{ms}$), resulting in a total duration of $59.77\,\mathrm{ms}$ for the full UE location procedure. During this time, the target can have a maximum absolute displacement of $0.12\,\mathrm{m}$, which is around 80% of the range resolution and would therefore result in neglectable range migration of only up to 0.80 radar range cells resolution. For the sake of completeness, other common radar signal processing performance parameters, including the maximum unambiguous range, maximum inter-symbol-interference (ISI) free range, relative radial velocity resolution, maximum unambiguous relative radial velocity, and maximum tolerable relative radial velocity calculated according to [4], [9] are also listed in Table I. The physical meaning of these parameters is explained in more detail in [46]. It could be visible that OCDM has some performance degradation, for example, in the velocity resolution. Nevertheless, the functionality of the system is not affected since OCDM in the proposed algorithm is an intermediate step. While OCDM is only used to detect whether any targets are present in the scanned flat-top angular sector, OFDM is combined with highly-directional beams to perform sensing for ultimately estimating the parameters of targets.

TABLE I: Adopted signal parameters and resulting radar performance parameters for OCDM flat top beam search and OFDM pencil beam search.

	OCDM flat top	**OFDM pencil beam**
RF parameters		
Bandwidth (B)	1 GHz	1 GHz
Carrier frequency (M)	26.2 GHz	26.2 GHz
Signal parameters		
No. of subchirps/subcarriers	2048	2048
Cyclic prefix length	0	512
No. of OCDM/OFDM symbols	512	1024
Single frame duration	1.05 ms	2.62 ms
Total measurement time	44.04 ms	15.73 ms
Radar performance parameters		
Processing gain (G_p)	60.21 dB	63.22 dB
Range resolution	0.15 m	0.15 m
Max. unamb. range	307.20 m	307.20 m
Max. ISI-free range	307.20 m	76.80 m
Rel. radial velocity resolution	5.46 m/s	2.18 m/s
Max. unamb. rel. radial velocity	1.40 km/s	1.12 km/s
Max. tolerable rel. radial velocity	279.55 m/s	279.55 m/s

B. RIS-JCAS Radar Image

First of all, the typical radar image after calibration is presented in Fig. 6(a) by processing the received signal from (9) using the experimental system in Fig. 5, based on the parameters listed in Table I. It could be visible that the strongest target with normalized magnitude $Mg = 0$dB exists at a distance of $R = 4.8\,\mathrm{m}$, null velocity v since the UE in Fig. 5 is stationary. It is important to notice that the measured distance contains all four path taps from the BS Tx to BS Rx mentioned in Fig. 1(a). Therefore, the value $r_\mathrm{RIS} = 4.65\,\mathrm{m}$ should be derived by subtracting the known distances $r_{p_1} = r_{p_4} = 0.15\,\mathrm{m}$ between the BS and RISs, which leads to the critical parameter to formulate the ellipsoid in Fig. 2 based on (18). The radar signal processing also detects the position of the RIS, which is presented by the second high value, which is 14dB weaker than the target and can be observed at $0.225\,\mathrm{m}$. This is because a practical RIS cannot fully reflect all the signals in the desired direction due to the existence of sidelobes and specular reflections mentioned in [12]. As a consequence, some coupling signals will also be propagated directly from the Tx RIS to the Rx, but travel a longer distance than $r_{p_1} + r_{p_4}$, which leads to the halved value of $0.225\,\mathrm{m}$. Since the RIS position is already known, this secondary target will not lead to the wrong detection, which can also be optionally calibrated. In addition, this path is the shortest propagation from Tx to Rx via a single RIS and, therefore, will not overlap with any valid UE detection. Besides the aforementioned targets, there are also other contributions along the y-axis at null velocity, which result from the signal reflections in RF circuits due to imperfect matching and the sinc-behaviour leakage when the target position is not exactly located at the discrete distance values [47]. Nevertheless, these values are at least 25dB weaker than the peak, which will not lead to any UE position estimation error.

C. Beam Training and Waveforms

Although the range and velocity information could be decently derived from the radar image, it does not provide the angle information to finalize the accurate UE position. As a solution, the beam training options mentioned in Section. III can be utilized to derive one range-velocity radar image for each beamforming pattern similar to Fig. 6(a). Gathering the peak value of such an image for all the beam pattern candidates will formulate an angle-dependent radar image. According to (10), the peak value will be higher with the beamforming directions closer to the UE yielding a higher G_RIS in (7), which finally influences the decisions of $\theta_\mathrm{b}, \phi_\mathrm{b}$ in (16). According to this idea, Fig. 6(b) shows the exhaustive high-directional beam search using OFDM radar signal processing covering the angle area in Section VI-A with $g_\mathrm{n} = 2^\circ$ for both dimensions. The suboptimum beam effect when forcing the identical beam for both RISs mentioned in Section. III will be more significant along the ϕ angle in Fig. 2. This is caused by the fact that the RIS spatial separation and the corner reflector width are both along the x-axis, where ϕ has more contributions according to the definitions in (19). This leads to the fact that there could be multiple beamforming angles, with their peak SNR values having small differences. By blindly trusting the absolute peak, accuracy could be lost since there could be unavoidable hardware imperfections that vibrate the radar SNR in (10). As a solution, this article proposes the idea of concluding that all the angles have less than a threshold T_r to the peak value based on the testbed performance analysis. Then, the determined beamforming directions will be the centre of the angle group in Fig. 6(b), which yields a practical alternative to the derivation of $\theta_\mathrm{b} = 14^\circ$ and $\phi_\mathrm{b} = 38^\circ$ for (16).

As discussed in Table I, the aforementioned full exhaustive search will significantly extend the total measurement time, which will lead to the unclear moving UE detection. Therefore, the flat-top beam hierarchical search mentioned in Section III is utilized, referring to the parameters in Section VI-A, with measurement results presented in Fig. 6(c). Here, $\boldsymbol{\theta}_\mathrm{f}$ has the $\theta_\mathrm{s} = 5^\circ$,$\theta_\mathrm{e} = 25^\circ$, with $g_{\mathrm{f},\theta} = 10^\circ$ as the angle resolution, which covers the same θ range from 0° to 30°. After the examination using (16), $\theta_\mathrm{f} = 15^\circ$ is chosen as the best flat-top beam. Then, according to algorithm 1, $\theta_\mathrm{s} = 10^\circ$,$\theta_\mathrm{e} = 20^\circ$, and $g_n = 2^\circ$ are updated for the exhaustive high-directional beam search using OFDM by repeating the corresponding range in Fig. 6(b), leading to $\theta_\mathrm{b} = 14^\circ$. For the decision of ϕ, it has no beam broadening, so the angles are examined exhaustively in Fig. 6(c), with the results slightly influenced due to the more scattered beamforming pattern, yielding the ϕ range from 34° to 44° based on T_r = 1dB. This leads to an average value of 39° which is not covered by the $g_\mathrm{n} = 2^\circ$ angle resolution, therefore, a comparison between 38° and 40° should be done, and the resulting higher value of 38° is chosen, which leads to the same result for the exhaustive beam case.

For further attempts, the flat-top beam broadens both angle dimensions using (17) can lead to a triangle shape as shown in Fig. 7(a). Such shaping offers a flexible construction by separating the entire beam training region into several quasi-isosceles triangles in Fig. 7(b). By rotating the coordinate in

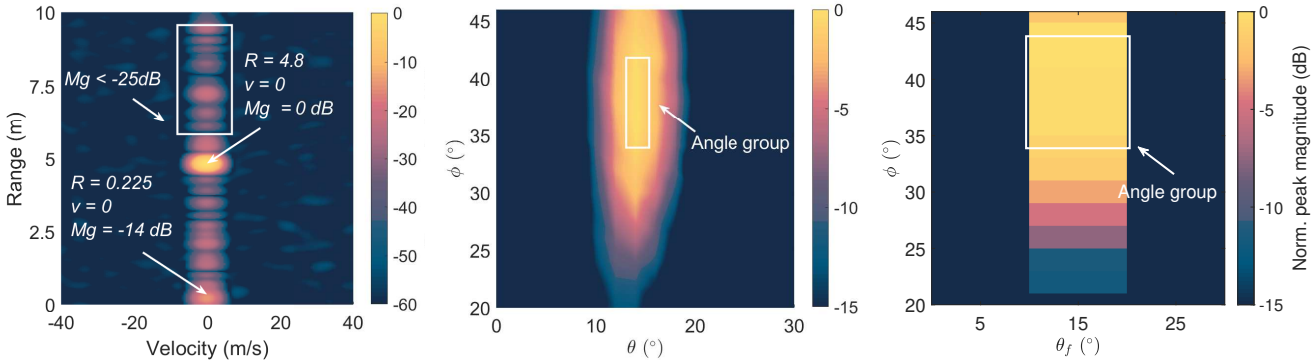

(a) (b) (c)

Fig. 6. RIS-JCAS radar images. (a) A range-velocity radar image with RIS beamforming. (b) An angle-dependent radar image generated through exhaustive high-directional beams with OFDM. The angle group covers $\phi = \phi_{\mathrm{Tx}} = \phi_{\mathrm{Rx}}$ from $34° : 2° : 42°$, and $\theta = \theta_{\mathrm{Tx}} = \theta_{\mathrm{Rx}} = 14°$. These angles have the T_r=1dB less magnitude than the peak, which are [-0.5, 0,-0,02,-0.08,-0.28]dB through the aforementioned ϕ values. (c) An angle-dependent radar image generated through 1D flat-top beams with OCDM. The angle group covers $\phi = \phi_{\mathrm{Tx}} = \phi_{\mathrm{Rx}}$ from $34° : 2° : 44°$, and $\theta_{\mathrm{f}} = \theta_{\mathrm{Tx}} = \theta_{\mathrm{Rx}} = 15°$. These angles have the T_r=1dB less magnitude than the peak, which are [-0.96,-0.4,-0,37,-0.39,0,-0.18]dB through the aforementioned ϕ values.

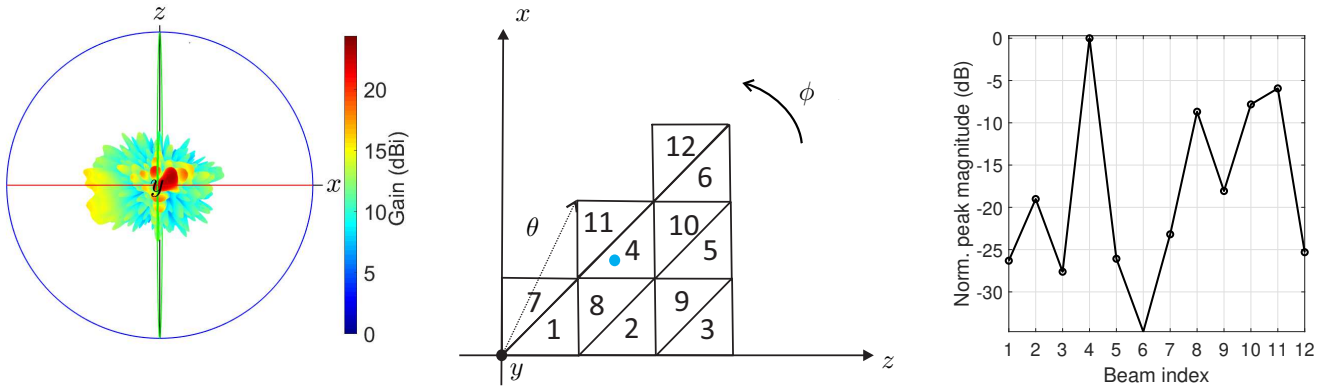

(a) (b) (c)

Fig. 7. Figures for triangle flat-top beam based RIS-JCAS analysis. (a) Simulated beamforming pattern of a 20×20 RIS with 1-bit phase resolution based on the prototype from [12] for the triangle flat-top beam with $B_{\mathrm{f}} = 3$ contributions $\phi_1 = 0°$,$\theta_1 = 7°$,$\phi_2 = 0°$,$\theta_2 = 0°$, and $\phi_3 = 45°$,$\theta_3 = 9°$. (b) Beam distribution using 12 triangle flat-top beams. The triangle vertices denote the sub-beams to formulate the flat-top beams. Angle ϕ is denoted by the tilting angle from the projection to z-axis, and θ is the angular distance to the y-axis. (c) Beam training results using triangle flat-top beams with OCDM.

Fig. 1(b), the isosceles triangle can be presented using angles, yielding each triangle having a waist of 7°, and a base of 9°. By using this novel spatial separation, the measurement effort can be further reduced by distributing the interested area into only 12 flat-top beams with each of the normalized radar image magnitudes depicted in Fig. 7(c). It is visible that beam index 4 has the highest magnitude, which correctly covers the UE located at the blue dots $\theta = 14°$ and $\phi = 38°$, which could be finalized using exhaustive high-directional beams. Overall, the cleverness of the proposed system is that the time efficiency benefits of the flat-top beam are realized without taking the risk of losing the UE or inaccurate sensing since the power loss is successfully compensated by using OCDM even with fewer symbols, as shown in Table. I.

D. Beam Fine-Tuning Results

Based on the results provided by the aforementioned measurements, the necessary parameters to formulate the beam fine-tuning constraints in (18) and (19) are derived. Using meter as unit, the TxIP at $(0.51, 4.47, 0.89)$ and RxIP at $(0.87, 4.52, 0.88)$ are obtained. To trace the UE range curve C(TxIP, RxIP) with the angle set in (20), ϕ angle has more variations and therefore is used as the axes for Fig. 8(a), while the values of $\boldsymbol{\theta}_{\mathrm{Tx,tune}}$ and $\boldsymbol{\theta}_{\mathrm{Rx,tune}}$ angles can be computed accordingly by keeping the same value along the convincible $z_c = 0.885$ with (19) and (18), yielding the value mostly within the coverage area of RIS beamforming to $14°$ in this measurement case. It is visible from Fig. 8(a) that the computed angle options from (20) with $\phi_{\mathrm{Tx}\to\mathrm{RxIP}} = 50°$, $\phi_{\mathrm{Rx}\to\mathrm{TxIP}} = 24°$ cover the optimum angle combination, which proves the correctness of the computed angle range in (20).

The exhaustive search measurement is an indication of the system performance, which is not desirable in practice, during which the UE would move away. As a comparison, when the proposed fine-tuning algorithm is utilized, the computed results regarding all the CPs are listed in Fig. 8(b). It is visible that the radar image magnitudes have very similar internal behaviour for each group due to the same changing ϕ_{Rx}, while the major external difference among the groups is the shift of magnitude due to the changing ϕ_{Tx}. By examining all the CPs with (21) in Fig. 8(b), the one who has the

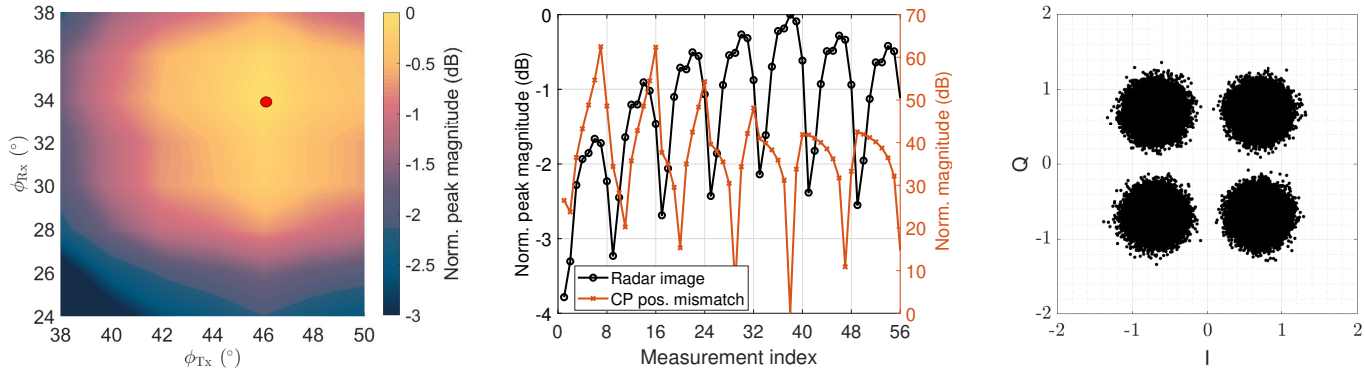

(a) (b) (c)

Fig. 8. Figures for fine-tuning results analysis. (a) Fine-tuning results observed with exhaustive search with OFDM considering $\boldsymbol{\phi}_{\mathrm{Tx,tune}} = [38° : 2° : 50°]$ and $\boldsymbol{\phi}_{\mathrm{Rx,tune}} = [24° : 2° : 38°]$ obtained from (20). The red dote denote the optimum angle combination with $\phi_{\mathrm{Tx}} = 46°$ and $\phi_{\mathrm{Rx}} = 34°$. The point $\phi_{\mathrm{Tx}} = \phi_{\mathrm{Rx}} = \phi_{\mathrm{b}} = 38°$ without any fine-tuning has the magnitude of -2.3dB. The minimum magnitude is -4dB at $\phi_{\mathrm{Tx}} = \phi_{\mathrm{b}} = 38°$, $\phi_{\mathrm{Rx}} = 24°$. (b) A comparison of radar image magnitude (black, left y-axis, transformation of the 2D results in (a) to 1D) and CP position mismatch (orange, right y-axis). The first measurement group with indexes 1 to 8 denotes the angle combinations with $\phi_{\mathrm{Tx}} = 38°$ and $\phi_{\mathrm{Rx}} \in [24° : 2° : 38°]$. For the next measurement group with indexes 9 to 16, $\phi_{\mathrm{Tx}} = 40°$ is used while the set of ϕ_{Tx} maintains. Following this logic, 56 angle combinations are listed until $\phi_{\mathrm{Tx}} = 50°$. (c) Recovered 314880 QPSK symbols of the proposed RIS-JCAS system covering the 400 MHz from 25.7 GHz to 26.1 GHz, based on the maximum bandwidth of n258 3GPP 5G standard centralized at 26 GHz.

TABLE II: Comparison of RIS-JCAS sensing and physically approximated results.

	RIS-JCAS sensing	**Approx. baseline**
UE position (x, y, z)	$(0.74, 4.5, 0.885)$m	$(0.75, 4.5, 0.9)$m
UE Range (r_{RIS})	4.65 m	4.65 m
Tx RIS DoD $(\theta_{\mathrm{Tx}}, \phi_{\mathrm{Tx}})$	$14°, 46°$	$15.8°, 45°$
Rx RIS DoA $(\theta_{\mathrm{Rx}}, \phi_{\mathrm{Rx}})$	$14°, 34°$	$13.5°, 33.7°$

minimum distance mismatch, which is also the determined UE location, is derived at index 38 which exactly corresponds to the measured $\phi_{\mathrm{Tx}} = 46°$ and $\phi_{\mathrm{Rx}} = 34°$. In Table II, the position of the UE, the radar sensed UE range and the final utilized DoD/DoA at RISs are compared with the approximated baseline corner reflector position measured with a laser pointer.

It can be seen in Table II that such comparisons are good indications of the system's feasibility, but there will always be some mismatches. They are in most practical times unavoidable due to the system hardware imperfection, RIS beamforming mismatch, laser measurement mismatch, etc. Nevertheless, in practice, it is more important to ensure that the signal propagation quality is guaranteed under the aforementioned effects. By observing the two curves in Fig. 8(b), there are a few interesting aspects worth noticing: first, the few minimum distance mismatch points correspond with the peak radar image magnitudes, which potentially increases the algorithm's robustness to utilize neighbour beamforming angles upon distortions. This correspondence becomes less accurate when the computed CP has angles largely biased toward the real UE position. This fact is caused by the limited radar range resolution, RIS angle resolution, and unavoidable hardware imperfections, leading to distorted input parameters for Alg.1. Fortunately, when the CP points are closer to the real UE position, or closer to the UE curve in Fig. 2, such biases might lead to determining the neighbouring RIS beamforming angles without large performance loss. When the CP points are far from the real UE position, for example, for the first two groups with index 1 to 16 having $\phi_{\mathrm{Tx}} = 36°$ or $38°$, any small input mismatch in the coordinate will be extended to larger errors. This also leads to the property that the distance mismatch in Fig. 8(b) can be regarded as a good indication of the system performance, but it has no formula-wise relationship to the radar image magnitude. Nevertheless, since such a loss of correspondence only exists for the wrong CP positions, the accuracy of the algorithm is not influenced. Second, the system may still encounter the risk that the global minimum value of (21) loses its accuracy due to system and environment variances. As a solution, instead of relying on a single measurement combination, the minimum position mismatch group can be selected, after which the best angle combination point within the group is determined. This alternation further increases the robustness of the RIS angle selection, focusing on the guarantee of signal propagation quality.

As a summary, the proposed algorithm in the novel RIS-JCAS system can provide proper RIS DoD/DoA determination proved by the measurement results. The position mismatch computation is utilized instead of time-consuming exhaustive beam searches, which realizes significant performance improvement to the furthest extent under practical system constraints, in comparison to directly using the sub-optimum angles provided by (16).

E. UE Communication Results

Once the beamforming directions of the RISs are finalized after the fine-tuning, the communication channel in (12) is also optimally established without any additional effort required. The only processing that needs to be done is a channel coefficient derivation using the pilot symbols at the UE to know the phase rotation of the incoming signals. This is also an efficient process since the same Tx signal structure can be kept for the JCAS system, which can be realized with the least

square estimation at each subcarrier. The recovered signal for the QPSK modulated symbols with low-density parity-check channel coding is given in Fig. 8(c). To obtain the SNR in (15), MER is used as a promising estimation, having a value of 14.37dB by averaging with 10 measurement rounds, which is a proper value for a $5\,\mathrm{m}$ link distance at mmWave frequency. For later signal processing, the Tx will keep the JCAS signal structure to realize the communication with the UE and sense its updated position information for mobile communication purposes.

VII. Practical Considerations

The proposed RIS-JCAS system in Fig. 1(a) is not strictly limited to one specific scenario. As mentioned in the research paper [32], the RIS applications toward 6G have variant possible specifications. To discuss further applications, practical considerations regarding different alternatives are discussed in this section.

A. BS and UE with Antenna Array

Antenna arrays can be equipped at the BS for a farfield illuminated RIS approach in Fig. 1(a). In this case, antenna arrays at BS will formulate the steering vector to illuminate the RIS, and the channel between the RIS and the BS array becomes a matrix. Nevertheless, if we jointly consider the effective channel by multiplying the aforementioned elements, the equivalent channel between the Tx to Tx RIS has the same vector format as $\boldsymbol{h}_p$. The additional array gain will be presented by α, and the reference point to determine RIS phases in (1) should consider the phase center of the utilized array. Therefore, the major system model as well as the later algorithm is kept the same. This change relates the RIS single antenna application case with the multiple antenna application case mentioned in [32].

B. RIS Specifications

The measurement results in this paper are mainly produced by utilizing the 1-bit RISs designed in [12], as a low-cost RIS that potentially offers the most marketing benefits. Nevertheless, it is also necessary to discuss further RIS specifications in case of future applications, such as the size of RIS, the RIS unit cell spacing, and their phase resolution. In principle, the channel model, algorithm, and simulation results proposed in this article already generalize the aforementioned specifications that ensure alternative RIS choices. Therefore, the possible changes in measurement results will be discussed using outcomes from Section VI as the benchmark.

For better analysis, the aforementioned specifications are concluded to have three major RIS beamforming properties, which are gain, beamwidth, and beam resolution. First, the change of gain alters the α terms in (10) and (15), which finally influence the radar image SNR values in Fig. 6(a) and the MER in Fig. 8(c). Therefore, it is necessary to ensure a proper gain over the cascaded channel to overcome the FSPL for qualified sensing and communication, which is a common requirement for wireless propagation systems. Second, the narrower beamwidth may increase the accuracy of the sub-optimum angle input from (16), since more clear changes in Rx power will reduce the number of angle candidates after the thresholding in Fig. 6. An accurate input to the fine-tuning algorithm will increase the final sensing and channel estimation accuracy. In addition, the magnitude difference in Fig. 8(a) will be more obvious if an exhaustive search is chosen. Last but not least, a better beam resolution not only provides more accurate derivation from (16), but also provides less angle quantization error for the final utilized RIS beamforming after the fine-tuning computation in Fig. 8(b).

C. LoS Path Between BS and UE

The system model in Fig. 1(a) follows the general reflective RIS channel mentioned in [32]. Nevertheless, it is worth mentioning that in the farfield illuminated RIS beamforming approach, studies are arguing that a LoS path between the BS and UE can also exist [23], [48]. In this case, RIS provides additional scattering in the wireless communication environment, which potentially increases the channel capacity. For the sake of completeness, the alternatives of the proposed algorithm under an existing BS to UE LoS path are worth discussing. In general, the entire algorithm can be kept when the following aspects are properly operated. First, the LoS path between the BS and UE will provide one additional path, which will be sensed by the radar signal processing, leading to another cluster in Fig. 6(a) due to the difference in propagation range. The magnitude of this cluster is independent of the angle during joint beam training and, therefore, can be easily recognized, and then subtracted from the radar image. After this processing, the leftovers of the radar image are only derived through the RIS reflected path, which leads to the same 4D sensing results as shown in Fig. 6(b). The final localization can also rely on the RIS-referred position without the necessity of taking the LoS distance into account. Nevertheless, the communication between BS and UE has to utilize both paths, and the solution was provided theoretically in [48] and experimentally evaluated in [36], by combining both estimated channel contributions with additional RIS phase tuning without influencing the beamforming pattern. Or, OFDM can be utilized to properly make use of the two paths as studied in [16], [49].

D. Distance Between UE and RIS

In practice, the UE may appear at different distances from the RIS point of view. As shown in Fig. 7(a), the angle mismatches of the proposed method are kept at a small value but could be still larger when r_{RIS} is smaller. In addition, the UE angular range as depicted in Fig. 2 could also be wider, which leads to more computation effort for the proposed algorithm or more measurement steps when the exhaustive search is utilized. Nevertheless, a UE close to the RIS will originally suffer from less FSPL, which means proper sensing and signal propagation performance even under the obstacles mentioned above. Following the behaviour in Fig. 7(a), the angle mismatch gets smaller with larger r_{RIS}, and the UE angular range in Fig. 18 also becomes smaller when the

radius of the ellipsoid grows larger. These properties lead to more efficient and accurate UE detection at a farther distance with a higher FSPL. For an extremely far UE case assuming sufficient Rx power, the fine-tuning algorithm may no longer be necessary. The sub-optimum angles from (16) become optimum solutions, and the RISs behave similarly to antenna elements with the same directional radiation patterns, with the size of the RISs and the space between them neglected.

VIII. Outlook and Conclusions

In this article, a novel RIS-JCAS system concept was proposed and its channel model was studied. Based on the channel, a sensing-assisted communication algorithm was created. A joint beam training process is realized, which increases the time efficiency significantly, considering RISs generating highly directional beams and flat-top beams. Besides the conventional OFDM, the OCDM waveform is utilized to ensure the sensitivity of the RIS-JCAS system when flat-top beams are utilized. The accuracy of the UE position is then further improved by a novel approach based on the 3D spatial ellipsoid theorem. The complexity of the 3D computation is reduced by using a 2D approximation approach with low mismatches, as proved by simulations. The aforementioned algorithm is further analyzed on a mmWave testbed with a bandwidth of 1 GHz centralized at 26.2 GHz. Overall, accurate 4D sensing results are derived, which strongly assists the communication channel estimation and realizes the core benefits of the proposed RIS-JCAS system.

References

[1] J. Hasch, E. Topak, R. Schnabel, T. Zwick, R. Weigel, and C. Waldschmidt, "Millimeter-wave technology for automotive radar sensors in the 77 GHz frequency band," *IEEE Trans. Microw. Theory Tech.*, vol. 60, no. 3, pp. 845–860, Mar. 2012.

[2] T. Hwang, C. Yang, G. Wu, S. Li, and G. Ye Li, "OFDM and its wireless applications: A survey," *IEEE Trans. Veh. Technol.*, vol. 58, no. 4, pp. 1673–1694, Aug. 2009.

[3] X. Ouyang and J. Zhao, "Orthogonal chirp division multiplexing," *IEEE Trans. Commun.*, vol. 64, no. 9, pp. 3946–3957, Sep. 2016.

[4] L. Giroto de Oliveira et al., "Discrete-Fresnel domain channel estimation in OCDM-based radar systems," *IEEE Trans. Microw. Theory Tech.*, vol. 71, no. 5, pp. 2258–2275, May 2023.

[5] M. Xiao et al., "Millimeter wave communications for future mobile networks," *IEEE J. Sel. Areas Commun.*, vol. 35, no. 9, pp. 1909–1935, Sep. 2017.

[6] E. Björnson, E. G. Larsson, and T. L. Marzetta, "Massive MIMO: ten myths and one critical question," *IEEE Commun. Mag.*, vol. 54, no. 2, pp. 114–123, Feb. 2016.

[7] Z. Lin, M. Lin, B. Champagne, W.-P. Zhu, and N. Al-Dhahir, "Secrecy-energy efficient hybrid beamforming for satellite-terrestrial integrated networks," *IEEE Trans. Commun.*, vol. 69, no. 9, pp. 6345–6360, 2021.

[8] T. Wild, V. Braun, and H. Viswanathan, "Joint design of communication and sensing for beyond 5G and 6G systems," *IEEE Access*, vol. 9, pp. 30 845–30 857, Feb. 2021.

[9] L. Giroto de Oliveira, B. Nuss, M. B. Alabd, A. Diewald, M. Pauli, and T. Zwick, "Joint radar-communication systems: Modulation schemes and system design," *IEEE Trans. Microw. Theory Tech.*, vol. 70, no. 3, pp. 1521–1551, 2022.

[10] T. J. Cui, M. Q. Qi, X. Wan, J. Zhao, and Q. Cheng, "Coding metamaterials, digital metamaterials and programmable metamaterials," *Light: Science & Applications*, vol. 3, no. 10, p. e218, 2014.

[11] M. Di Renzo, M. Debbah, D.-T. Phan-Huy, A. Zappone, M.-S. Alouini, C. Yuen, V. Sciancalepore, G. C. Alexandropoulos, J. Hoydis, H. Gacanin *et al.*, "Smart radio environments empowered by reconfigurable AI meta-surfaces: an idea whose time has come," *EURASIP Journal on Wireless Communications and Networking*, vol. 2019, no. 1, pp. 1–20, 2019.

[12] X. Wan, Q. Xiao, Y. Z. Zhang, Y. Li, J. Eisenbeis, J. W. Wang, Z. A. Huang, H. X. Liu, T. Zwick, and T. J. Cui, "Reconfigurable sum and difference beams based on a binary programmable metasurface," *IEEE Antennas Wireless Propag. Lett.*, vol. 20, no. 3, pp. 381–385, 2021.

[13] L. Di Palma, A. Clemente, L. Dussopt, R. Sauleau, P. Potier, and P. Pouliguen, "1-bit reconfigurable unit cell for Ka-band transmitarrays," *IEEE Antennas Wireless Propag. Lett.*, vol. 15, pp. 560–563, 2015.

[14] L. G. da Silva, P. Xiao, and A. Cerqueira, "A 2-bit tunable unit cell for 6G reconfigurable intelligent surface application," in *2022 16th European Conference on Antennas and Propagation (EuCAP)*. IEEE, 2022, pp. 1–5.

[15] Y. Li, S. Bettinga, J. Eisenbeis, J. Kowalewski, X. Wan, X. Long, T. Li, A. Jauch, T. Cui, and T. Zwick, "Beamsteering for 5G mobile communication using programmable metasurface," *IEEE Wireless Communications Letters*, 2021.

[16] Y. Li, X. Long, L. Giroto de Oliveira, J. Eisenbeis, M. B. Alabd, S. Bettinga, X. Wan, T. J. Cui, and T. Zwick, "Programmable metasurface hybrid MIMO beamforming: Channel estimation, data transmission, and system implementations at 28 GHz," *IEEE Systems Journal*, 2022.

[17] Q. Wu, S. Zhang, B. Zheng, C. You, and R. Zhang, "Intelligent reflecting surface aided wireless communications: A tutorial," *IEEE Trans. Commun.*, 2021.

[18] X. Ma, S. Guo, H. Zhang, Y. Fang, and D. Yuan, "Joint beamforming and reflecting design in reconfigurable intelligent surface-aided multi-user communication systems," *IEEE Trans. Wireless Commun.*, vol. 20, no. 5, pp. 3269–3283, 2021.

[19] J. Zhang, E. Björnson, M. Matthaiou, D. W. K. Ng, H. Yang, and D. J. Love, "Prospective multiple antenna technologies for beyond 5G," *IEEE J. Sel. Areas Commun.*, vol. 38, no. 8, pp. 1637–1660, Aug. 2020.

[20] Z. Lin, M. Lin, T. De Cola, J.-B. Wang, W.-P. Zhu, and J. Cheng, "Supporting iot with rate-splitting multiple access in satellite and aerial-integrated networks," *IEEE Internet of Things Journal*, vol. 8, no. 14, pp. 11 123–11 134, 2021.

[21] Z. Lin, H. Niu, K. An, Y. Wang, G. Zheng, S. Chatzinotas, and Y. Hu, "Refracting ris-aided hybrid satellite-terrestrial relay networks: Joint beamforming design and optimization," *IEEE Trans. Aerosp. Electron. Syst.*, vol. 58, no. 4, pp. 3717–3724, 2022.

[22] Z. Lin, H. Niu, K. An, Y. Hu, D. Li, J. Wang, and N. Al-Dhahir, "Pain without gain: Destructive beamforming from a malicious ris perspective in iot networks," *IEEE Internet of Things Journal*, 2023.

[23] Y. Li, S. Bettinga, F. Gedenk, X. Long, M. B. Alabd, L. G. de Oliveira, and T. Zwick, "Experimental study of channel estimation algorithms for general IRS applications," in *2023 17th European Conference on Antennas and Propagation (EuCAP)*. IEEE, 2023, pp. 1–5.

[24] Y. Li, J. Eisenbeis, X. Wan, S. Bettinga, X. Long, M. B. Alabd, J. Kowalewski, T. J. Cui, and T. Zwick, "A programmable metasurface based TDMA fast beam switching communication system at 28 GHz," *IEEE Antennas Wireless Propag. Lett.*, 2021.

[25] Z. Esmaeilbeig, K. V. Mishra, and M. Soltanalian, "IRS-aided radar: Enhanced target parameter estimation via intelligent reflecting surfaces," in *2022 IEEE 12th Sensor Array and Multichannel Signal Processing Workshop (SAM)*, Jun. 2022, pp. 286–290.

[26] Z. Esmaeilbeig, A. Eamaz, K. V. Mishra, and M. Soltanalian, "Moving target detection via multi-IRS-aided OFDM radar," in *2023 IEEE Radar Conference (RadarConf23)*, May 2023, pp. 1–6.

[27] A. M. Elbir, K. V. Mishra, M. R. B. Shankar, and S. Chatzinotas, "The rise of intelligent reflecting surfaces in integrated sensing and communications paradigms," *IEEE Network (Early Access)*, pp. 1–8, Dec. 2022.

[28] L. Wang, L. F. Abanto-Leon, and A. Asadi, "Joint communication and sensing in ris-enabled mmwave networks," *arXiv preprint arXiv:2210.03685*, 2022.

[29] C. K. Sheemar, G. C. Alexandropoulos, D. Slock, J. Querol, and S. Chatzinotas, "Full-duplex-enabled joint communications and sensing with reconfigurable intelligent surfaces," *arXiv preprint arXiv:2306.10865*, 2023.

[30] X. Fang, W. Feng, Y. Chen, N. Ge, and Y. Zhang, "Joint communication and sensing toward 6g: Models and potential of using mimo," *IEEE Internet of Things Journal*, vol. 10, no. 5, pp. 4093–4116, 2022.

[31] W. Tang, M. Z. Chen, X. Chen, J. Y. Dai, Y. Han, M. Di Renzo, Y. Zeng, S. Jin, Q. Cheng, and T. J. Cui, "Wireless communications with reconfigurable intelligent surface: Path loss modeling and experimental measurement," *IEEE Trans. Wireless Commun.*, vol. 20, no. 1, pp. 421–439, 2020.

[32] J. Xu, C. Yuen, C. Huang, N. Ul Hassan, G. C. Alexandropoulos, M. Di Renzo, and M. Debbah, "Reconfiguring wireless environments via

intelligent surfaces for 6g: reflection, modulation, and security," *Science China Information Sciences*, vol. 66, no. 3, p. 130304, 2023.

[33] L. Zhang, M. Z. Chen, W. Tang, J. Y. Dai, L. Miao, X. Y. Zhou, S. Jin, Q. Cheng, and T. J. Cui, "A wireless communication scheme based on space-and frequency-division multiplexing using digital metasurfaces," *Nature Electronics*, vol. 4, no. 3, pp. 218–227, 2021.

[34] J. Xu, W. Xu, D. W. K. Ng, and A. L. Swindlehurst, "Secure communication for spatially sparse millimeter-wave massive mimo channels via hybrid precoding," *IEEE Trans. Commun.*, vol. 68, no. 2, pp. 887–901, 2019.

[35] A. Alkhateeb, O. El Ayach, G. Leus, and R. W. Heath, "Channel estimation and hybrid precoding for millimeter wave cellular systems," *IEEE journal of Sel. Topics Signal Process.*, vol. 8, no. 5, pp. 831–846, 2014.

[36] Y. B. Li, X. Wan, B. G. Cai, Q. Cheng, and T. J. Cui, "Frequency-controls of electromagnetic multi-beam scanning by metasurfaces," *Scientific reports*, vol. 4, no. 1, pp. 1–7, 2014.

[37] Y. Li, X. Long, X. Wan, J. Eisenbeis, S. Bettinga, T. Cui, and T. Zwick, "Realization of efficient channel estimation using programmable metasurface," in *2021 IEEE USNC-URSI Radio Science Meeting (Joint with AP-S Symposium)*. IEEE, 2021, pp. 66–67.

[38] W. Xu, Z. Yang, D. W. K. Ng, M. Levorato, Y. C. Eldar, and M. Debbah, "Edge learning for b5g networks with distributed signal processing: Semantic communication, edge computing, and wireless sensing," *IEEE journal of selected topics in signal processing*, vol. 17, no. 1, pp. 9–39, 2023.

[39] V. Savaux, "Flexible communication system for 6G based on orthogonal chirp division multiplexing," in *2022 1st Int. Conf. 6G Netw.*, Jul. 2022, pp. 1–5.

[40] L. Giroto de Oliveira et al., "Bistatic OFDM-based joint radar-communication: Synchronization, data communication and sensing," in *2023 20th European Radar Conference (EuRAD)*, 2023, pp. 359–362.

[41] B. Nuss, J. Mayer, S. Marahrens, and T. Zwick, "Frequency comb ofdm radar system with high range resolution and low sampling rate," *IEEE Transactions on Microwave Theory and Techniques*, vol. 68, no. 9, pp. 3861–3871, 2020.

[42] B. Zheng and R. Zhang, "Intelligent reflecting surface-enhanced ofdm: Channel estimation and reflection optimization," *IEEE Wireless Communications Letters*, vol. 9, no. 4, pp. 518–522, 2019.

[43] X. Wan, M. Q. Qi, T. Y. Chen, and T. J. Cui, "Field-programmable beam reconfiguring based on digitally-controlled coding metasurface," *Scientific reports*, vol. 6, p. 20663, 2016.

[44] Y. Li, "Intelligent reflecting surfaces in wireless communication systems," Ph.D. dissertation, Dissertation, Karlsruhe, Karlsruher Institut für Technologie (KIT), 2023, 2023.

[45] A. Forde and J. Daniel, "Pedestrian walking speed at un-signalized mid-block crosswalk and its impact on urban street segment performance," *Journal of traffic and transportation engineering (English edition)*, vol. 8, no. 1, pp. 57–69, 2021.

[46] B. Nuss, J. Mayer, and T. Zwick, "Limitations of MIMO and multi-user access for OFDM radar in automotive applications," in *2018 IEEE MTT-S International Conference on Microwaves for Intelligent Mobility (ICMIM)*, 2018, pp. 1–4.

[47] L. Giroto de Oliveira, T. Antes, B. Nuss, E. Bekker, A. Bhutani, A. Diewald, M. B. Alabd, Y. Li, M. Pauli, and T. Zwick, "Doppler shift tolerance of typical pseudorandom binary sequences in pmcw radar," *Sensors*, vol. 22, no. 9, p. 3212, 2022.

[48] C. You, B. Zheng, and R. Zhang, "Intelligent reflecting surface with discrete phase shifts: Channel estimation and passive beamforming," in *ICC 2020-2020 IEEE International Conference on Communications (ICC)*. IEEE, 2020, pp. 1–6.

[49] Y. Li, S. Bettinga, X. Long, M. B. Alabd, L. G. de Oliveira, and T. Zwick, "Experimental study of channel estimation and transmit diversity for irs-based miso system," in *2023 53rd European Microwave Conference (EuMC)*. IEEE, 2023, pp. 202–205.